Lawrence Berkeley National Laboratory
Recent Work

Title

ENERGY-MASS DISTRIBUTION AND ANGULAR MOMENTUM EFFECTS IN HEAVY-ION-INDUCED FISSION

Permalink

https://escholarship.org/uc/item/0wg6g8nh

Author

Plasil, Franz.

Publication Date

1964-12-31

University of California

Ernest O. Lawrence Radiation Laboratory

ENERGY-MASS DISTRIBUTIONS AND ANGULAR MOMENTUM EFFECTS IN HEAVY-ION-INDUCED FISSION

Berkeley, California

DISCLAIMER

UNIVERSITY OF CALIFORNIA

Lawrence Radiation Laboratory
Berkeley, California

Contract No. W-7405-eng-48

ENERGY-MASS DISTRIBUTIONS AND ANGULAR MOMENTUM
EFFECTS IN HEAVY-ION-INDUCED FISSION

Franz Plasil

(Ph. D. Thesis)

December 31, 1963

ENERGY-MASS DISTRIBUTIONS AND ANGULAR MOMENTUM
EFFECTS IN HEAVY-ION-INDUCED FISSION

Contents

ENERGY-MASS DISTRIBUTIONS AND ANGULAR MOMENTUM EFFECTS IN HEAVY-ION-INDUCED FISSION

Franz Plasil

Lawrence Radiation Laboratory
University of California
Berkeley, California

December 31, 1963

ABSTRACT

This work involves measurements of the energy and mass distributions of fission fragments produced by the bombardment of a number of relatively light elements with heavy ions. The results have been interpreted in terms of an approximate version of the liquid drop model which applies to this region of elements. The energies of both fission fragments from every event considered have been measured with solid state detectors, and recorded in a correlated manner. The energy data has been transformed to give mass-total kinetic energy density-of-events distributions. The reactions studied were (a) $Er^{170} + O^{16} = Os^{186}$, (b) $Yb^{174} + C^{12} = Os^{186}$, and (c) $W^{182} + O^{16} = Pb^{198}$. Data at several bombarding energies in each case have been obtained. Comparisons with quantitative liquid drop calculations were made and good agreement was found in the gross features of the distributions, and in the nuclear temperature dependence of the widths. Fission cross sections have been calculated by evaluating fission widths, and fitted to measured cross section data. From the parameters used in these fits, average values for the nuclear temperature of the

fissioning nuclei have been obtained. The fission barriers
needed for these calculations have been obtained from calcu-
lated energies of deformation of rotating charged liquid
drops in their equilibrium configurations.

I. INTRODUCTION

Since the discovery of fission almost a quarter of a century ago, no theory has been developed that is capable of explaining all the complex phenomena of this process. One of the methods that has evolved is to regard the nucleus as an incompressible drop of a uniformly charged liquid. Even such a simple model becomes complicated when applied to fission. For a long time difficulties lay in finding an adequate set of coordinates for describing the liquid drop, and in the complexity of the calculations once a parametrization had been selected. It is only within the last two years that the deformation energies and the shapes of the saddle configurations have been accurately calculated.[1,2] One of the results of these calculations was a rather natural division of the fission phenomena into those above $x \simeq 0.67$ and those below this value. (For a definition of the fissionability parameter, x, see footnote 32.) This division is due to the fact that the saddle configurations have a pronounced neck in the region of $x \lesssim 0.67$. This makes it possible in principle to relate the shape at scission to the shape at the saddle. Therefore, even though the liquid drop model cannot in its present state of development account for many observed effects in the region of $x \gtrsim 0.67$, it may be of value for interpretation of the fission of elements lighter than radium. The necked-in nature of the saddle shapes in the region of

$x \lesssim 0.67$ made it possible to consider the nucleus as two
spheroids (either overlapping, or tangent to each other)
without the loss of the general features of the liquid drop
model. This approximation has made calculations considerably
easier, and Nix and Swiatecki[3] have used it in calculating
mass-total kinetic energy distributions, which may be com-
pared directly with experiments, without the use of any
adjustable parameters. Such comparisons have been made
recently by Burnett.[4] The purpose of this work is to make
further measurements and comparisons with the work of Nix
and Swiatecki, over a range of values of x and excitation
energies.

To induce fission of such relatively light elements
as is required for comparison with theory, use of those
effects must be made which increase the fission probability.
Two of these are

(a) high excitation energy

(b) high angular momentum.

In this work, use has been made of both effects by inducing
fission with heavy ions. Each has brought with it complica-
tions, which in turn had to be considered. For example, at
high excitation energies, fission following neutron emission
may be important, and due to a distribution of angular
momenta obtained in bombardments with heavy ions, the fission
threshold (a function of angular momentum) for any given

bombardment is no longer one well-defined number. Both of these effects tend to make the excitation energy at the saddle uncertain. Calculations involving both effects are presented in the theoretical section.

The experimental method used was the simultaneous measurement of the energies of both fission fragments produced in the fission of a highly excited compound nucleus. These types of measurements, using heavy ions to produce the compound nucleus, were first made by Haines,[5] and the procedure used in this work is quite similar to that used by him.

The law of conservation of linear momentum makes it possible to calculate the mass of a fragment provided the energies of both fragments from that event are known. Thus, it is possible to present the data in terms of the probability of observing an event in which the total kinetic energy released is E_T, and in which one fragment has a mass A_1. Since the law of conservation of linear momentum applies strictly only to the fragments before they emit neutrons, and because the energy measurements are made after the emission has taken place, the transformation is only approximate. The error introduced is negligible, however, and will be discussed more fully in Section III and Appendix C.

The two compound nuclei studied were Os^{186} and Pb^{198}. They were produced with several excitation energies in the

following ways:

$$_{68}Er^{170} + {_8}O^{16} \longrightarrow {_{76}}Os^{186*}$$

$$_{70}Yb^{174} + {_6}C^{12} \longrightarrow {_{76}}Os^{186*}$$

$$_{74}W^{182} + {_8}O^{16} \longrightarrow {_{82}}Pb^{198*}$$

The reaction
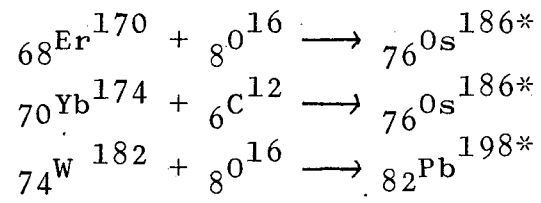
$$_{79}Au^{197} + {_2}He^4 \longrightarrow {_{81}}Tl^{201*} \longrightarrow \text{fission}$$
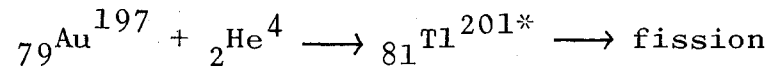
has also been studied, using helium ions of 70 MeV.[6]

Various features of the energy-mass distributions have been studied and compared with the theory of Nix and Swiatecki.

II. EXPERIMENTAL

A. Mechanical

1. Apparatus

The chamber used in this work has been extensively described elsewhere.[4,5,8] The heavy ion beam, defined by two circular collimators of 2 mm diameter and 60 cm apart, strikes a target at the center of the chamber. Two solid state detectors mounted on arms, that can be rotated from the outside of the chamber, measure the fragment energies. The center-of-mass transformation procedure[5] requires the definition of the angle of one of the fission fragments. This was done by placing one of the detectors at an angle of about 60° with respect to the beam direction, and at a sufficient distance from the target, so that the angle subtended at the center was about 3°. This angle is optimum because it allows a reasonable counting rate without introducing a large dispersion due to angular uncertainty. The other detector was placed at a distance of 1.2 in. from the target, and was collimated by a 3/8 in. x 9/16 in. rectangle. Such a large detector is thought to be able to collect all fission fragments in coincidence with those in the first detector.[9] The angular position of the large detector is typically 90° with respect to the beam direction. Its exact position was determined for each bombardment by a rough angular correlation experiment. In this angular arrangement the counting rate

in the two detectors is approximately equal. The beam is collected on a Faraday cup with a magnet at its entrance to eliminate interference from delta rays. Magnets were also placed in front of the two detectors in order to eliminate interference from low energy electrons.

2. Beam

Heavy ion beams of 10.3 ± 0.1 MeV per nucleon[10] energy were obtained from the Berkeley Heavy Ion Linear Accelerator (Hilac). Aluminum foils were used to degrade the beam energy when needed. The energies were estimated by means of range-energy curves of Northcliffe.[11] It was found necessary to maintain beam levels of less than 20 mμa due to a large loss of resolution at higher levels. Resolution was checked occasionally by measuring spectra at different beam levels, as well as continuously by inspecting the position and width of a spectrum of pulses from a pulse generator.

B. Target Preparation

Enriched isotopes of Er^{170}, Yb^{174}, and W^{182} were obtained in the oxide form from the Oak Ridge National Laboratory. The oxide was converted to fluoride by precipitation from nitric acid solution. The targets were prepared from the fluoride by electron bombardment.[7] The Au and Bi targets were prepared by vaporization of the pure metal. In all cases the deposition was made onto commercial thin Ni foils. Table II-1 gives values of the percentage enrichment and nominal

Table II-1. Thickness and enrichment of targets.

Target	Target thickness $(\mu\mathrm{g}/\mathrm{cm}^2)$	Backing thickness $(\mu\mathrm{g}/\mathrm{cm}^2)$	Enrichment %
Er^{170}	207	113	87.3
Yb^{174}	186	113	98.97
W^{182}	174	113	94.4
Au^{197}	200	90	–
Bi^{209}	110	90	–

thickness of the targets. Nominal thicknesses were obtained by weighing, and enrichment values have been furnished by the isotope suppliers.

C. Detectors

Surface-barrier gold-silicon solid state detectors of the type first described by Blankenship[12] were used. The resistivity of the silicon was 150-Ω-cm and they were operated at a reverse bias of about 10-15 V. At this bias all fission fragments are stopped in the depletion layer, but the scattered heavy ions, which cause an undesirable background of pulses, do not deposit all of their energy. The detectors showed the familiar nonproportionality effects discussed extensively elsewhere.[13] The final method of calibration and correction for this effect is described in Section III-A. The choice is based largely on the experience of Haines[5] and Burnett,[4] who used similar detectors for similar measurements. The following two calibration measurements were made during the course of each experiment:

(a) The coincidence fission spectrum of Cf^{252} was measured and recorded by the entire experimental system. No settings were changed after these data had been gathered. The same measurement was repeated at the end of the experiment. This was also a check on the stability of the electronic system and on the deterioration of detectors due to radiation damage.

(b) Due to large center-of-mass effects in bombardments with heavy ions, the average fragment lab energy varies; in the case of $Bi^{209} + O^{16}$ for example, from 104 MeV when measured at an angle of 50° with respect to the beam direction to 51 MeV when measured at an angle of 140°. Use of this effect for calibration purposes has been made by other workers.[5,14] Measurements of singles spectra were made in both detectors at about five different angles during each experiment. The most probable energies were taken from the work of Viola and Sikkeland.[15]

Leakage current in the detectors was continuously monitored during each run. It was found to increase rapidly when radiation damage became appreciable. Typically the leakage current was between 0.2 and 1 μa. Currents greater than 3 μa were not tolerated.

D. Electronics

The electronic equipment used was similar to that of Haines[5] and is described in some detail in Appendix A. It consists of a fast coincidence system (FC), a fast-slow coincidence system (FSC), and a linear system. The FSC system requires a coincidence between two slow linear pulses and the delayed output from the FC system. The FC system was found to be necessary due to the high background of scattered heavy ions. The FSC system output serves as a

trigger to activate a two-dimensional pulse-height analyzer which analyzes individually the linear pulses and stores them in correlated form on magnetic tape. Aside from the nonproportionality effects mentioned earlier, the pulses recorded by the analyzer represent the energies of the fission fragments. Thus both fragment energies from every fission event observed are measured, and the data are stored on tapes that are compatible with IBM computers and allow direct data processing. The fission spectra are also monitored on two pulse-height analyzers in uncorrelated form. A pulse generator sends pulses through the whole system at the rate of about ten per minute to check for electronic drift and loss of resolution due to high beam intensity. Figure A in the appendix gives the block diagram of the electronic system.

E. Data Collection

The experiments were carried out over a period of several months. A total of seven experiments yielded the data used in this work. Table II-2 gives the total number of events gathered for the various systems and bombarding energies. The numbers of experiments are also given. In cases where data of one type were gathered in several experiments, they were added together on the computer for the final presentation of results. The following should be noted:

Table II-2. Number of fission events measured.

System	Projectile energy (MeV)	Experiment number	Number of events per experiment
$_{68}Er^{170} + _8O^{16}$	120	4	25,000
	120	6	21,000
	136	3	26,000
	136	7	44,000
	151	2	27,000
	165	1	53,000
	165	6	37,000
	165	7	62,000
$_{70}Yb^{174} + _6C^{12}$	125	5	31,000
	109	5	21,000
$_{74}W^{184} + _8O^{16}$	102	6	38,000
	115	7	41,000
	127	6	43,000
	144	7	110,000
	165	6	102,000

(a) The Er^{170} + O^{16} data were gathered during many different experiments. Only in one case was there no addition of data from several experiments. In this case (bombarding energy of 151 MeV) the statistics were not very good. An experimental difficulty was presented by the relatively low fission cross sections in these reactions, which did not allow rapid collection of a large number of events in the period of an average experiment length of 20 hrs. This problem was compounded by the necessity to keep beam levels low for good resolution and to avoid "gain-shift" between in-beam and out-of-beam operation.[14]

(b) The problem of low cross sections was even greater in the case of carbon-induced fission of ytterbium. Statistics were poor and beam levels had to be kept somewhat higher than in the erbium case.

(c) All the tungsten data were collected during the course of two experiments. Statistics were good, and no addition of data from different experiments was necessary. It was possible to operate at very low beam currents due to the increased fission cross section.

III. CALCULATIONS AND DATA PROCESSING

This section is intended to cover the discussion of the procedure necessary to transform the data obtained from the two-dimensional pulse-height analyzer into its final form (mass and kinetic energy distributions) in which the results can be compared with theory. Thus, we discuss here the choice of a calibration scheme, miscellaneous corrections such as those due to target thickness, center-of-mass transformations, and the effects introduced by the evaporation of neutrons before and after fission. Certain definitions of energy terms such as "excitation energy" will be introduced in this section. If further clarification of these terms is necessary, a more detailed discussion will be found in Section IV-A and Fig. IV-1, which also includes a discussion of theoretical terminology.

A. Choice of Calibration Scheme

In the absence of nonproportionality effects, the energy E_1 of a fission fragment would be related to the pulse height V, that it induces, by the simple linear relationship

$$E_1 = a + bV \quad , \qquad (III-1)$$

where a and b are constants. Since the most commonly observed nonproportionality effects are such that fragments of equal energy but of different mass do not produce the

same pulse height, Eq. (III-1) may be rewritten as

$$E_1 = a(A_1) + b(A_1)V \quad . \qquad (III-2)$$

The following calibration schemes, described in greater detail in reference 4 have been reconsidered here.

1. Two Peak (TP) Calibration Scheme

This scheme neglects all mass dependence, i.e. $a(A_1) = a_0$ and $b(A_1) = b_0$ in Eq. (III-2). The coefficients a_0 and b_0 can be evaluated by fitting to the two peaks of well known energy from the spontaneous fission of Cf^{252}. Time-of-flight overall averages tabulated in reference 4 were used as standard energies. This method gives extreme values for the two constants, a_0 being larger than in all other calibration schemes and b_0 being smaller. If the open circles in Fig. III-1 represent the two peaks of Cf^{252}, then the solid line represents the TP scheme. The line is the same for all masses.

2. Common Intercept (CI) Calibration Scheme

This case represents the other extreme. Pulse-height energy curves consist of a family of lines all having a common intercept at V=0 $\left[i.e. \ a(A_1) = 0\right]$. The slopes increase linearly with mass $\left[b(A_1) = b_0 + b_1(A_1-106)\right]$. The constants b_1 and b_0 are again obtained from Cf^{252} spontaneous fission data. The pulse-height versus energy curves for the most probable light fragment mass (106) and the most probable heavy fragment mass (146) in Cf^{252} fission are shown by the
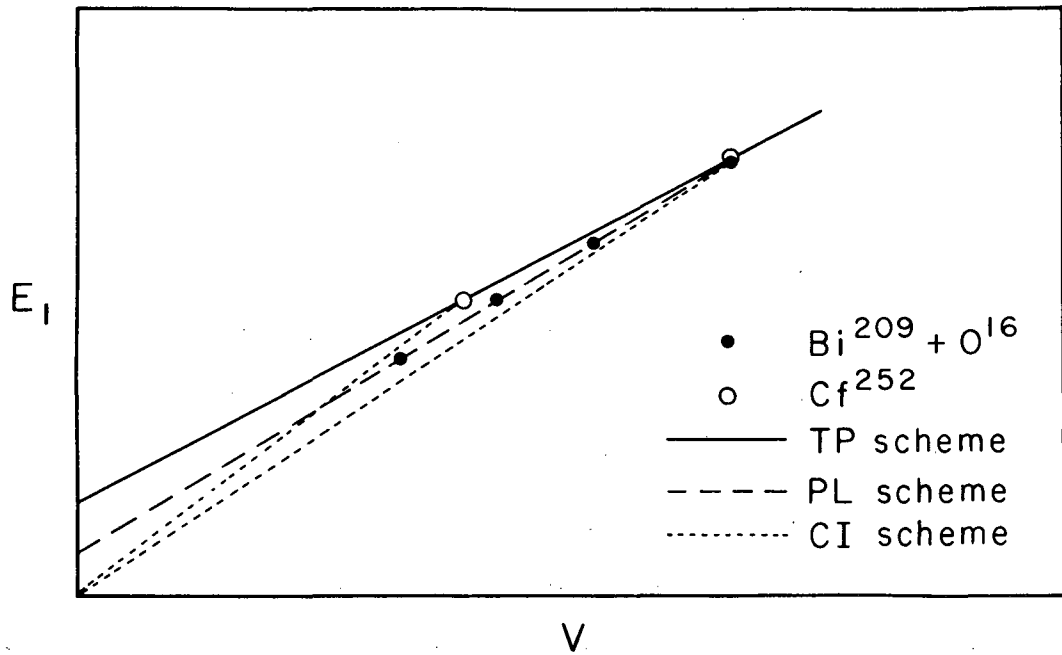
Figure III-1. Schematic illustration of various calibration schemes.

dotted lines in Fig. III-1.

3. Parallel Line (PL) Scheme

In this scheme the pulse-height energy curves for all masses have the same slope, and the dependence of the intercept on mass is linear, i.e. $[a(A_1) = a_o + a_1(A_1-106)]$.

The constants a_1 and a_o can be evaluated from Cf^{252} data. The slope of the family of parallel lines is obtained from data on the fission of bismuth with oxygen ions (see Section II-C). These data consist of a set of measured pulse heights and corresponding known energies.[15] The mass is the same for each point, being simply the most probable mass in the fission of the compound nucleus $_{91}Pa^{225}$ produced in the bombardment of $_{83}Bi^{209}$ with $_8O^{16}$. These data are represented by closed circles in Fig. III-1. Thus the broken line in this figure represents the relationship between pulse-height and energy for a mass of about 110. The curves for heavier fragments lie above the line, and those for lighter fragments lie below.

The PL scheme was chosen for the same resons given by Burnett in reference 4. He has used the 6.1 MeV α-particles from Cf^{252} to define the slope of the parallel lines. The same tests that he has performed on the three calibration schemes have been carried out. The conclusions are identical, and the PL scheme based on the Bi fission data gives almost the same results as the PL scheme based on the Cf^{252} alpha

particle data.

Due to the lower total kinetic energy of the fission reactions considered here, the differences between the various calibration schemes are greater than in the work of Burnett. Thus in the case of $Er^{170} + O^{16}$, $\langle E_T^* \rangle$, the average total kinetic energy of fragments before correction for neutron emission, ranges from 115 MeV using the CI calibration method to 130 MeV when the TP method is used. The corresponding energy in the PL scheme is 120 MeV. Furthermore, in the TP scheme the spectra from the two detectors do not correspond in energy after the center-of-mass transformation is made, indicating that serious error is introduced by this scheme. In general it was found that the energy spectra from the two detectors were in best agreement when the PL scheme was used.

It should be emphasized that the largest error caused by the uncertainty in calibration is in E_T, the total kinetic energy released. The error in the width of the E_T-yield distribution is considerably smaller, and the error in the width of the mass-yield distribution is almost negligible when the PL scheme is used, as can be seen from reference 4. The errors due to calibration uncertainty were taken into account when the final errors of all measured quantities were estimated. The important conclusion is that mass-yield curves obtained from detector measurements do not suffer

appreciably from the effects of nonproportionality.

B. Correction for Electronic Drift

Due to the low fission cross sections for the
reactions considered here, the time required to measure a
mere 30,000 fission events could be as much as six hours.
During such a long period of time, the possibility of
electronic drift occurring was quite high. A mercury pulse
generator (sending pulses at the rate of about 10 per
minute through the whole system) was used to check the
electronic stability. The pulses from the generator were
recorded in the two-dimensional analyzer in the usual manner,
but a special mark on the tape distinguished them from
fission events. Thus it was possible to follow the drift
throughout the experiment and to correct for it continuously.
The correction was found to be small, never exceeding 2%.
In most cases, the correction was altogether negligible. An
independent check on electronic stability was also avail-
able in the form of a comparison of Cf^{252} fission data
before and after each experiment.

C. Target Thickness Correction

The functional form of the energy loss ΔE_t due to
the finite thickness of the target was taken to be

$$\Delta E_t = c E^{1/3} \tag{III-3}$$

for a fragment of energy E. This equation is based on the

results of Alexander and Gazdik.[22] From their work one may also conclude that the dependence on mass of the constant c in the above equation is small. The constant c was evaluated experimentally as follows: coincidence data were collected in three positions of the target.

(a) The plane of the target at 90° to detector 1, the target material facing it.

(b) The plane of the target rotated by 60° (target material still facing detector 1).

(c) As in (a), but the nickel backing facing detector 1. From the shifts of the peak from one position to another, the constant c was deduced for both sides of the target, and all subsequent data obtained with the target were corrected. Due to the relatively low statistics of the coincidence measurements, it is believed that the correction is good to only about 15%. Since ΔE_t is of the order of 5 MeV, an error in the measured energy of up to ±0.8 MeV may result. The dispersion introduced in the final distribution due to the uncertainty as to where within the target the event originates has been shown by Haines[5] to be small and has therefore been neglected.

D. Center-of-Mass Correction

This correction is important in magnitude in reactions studied here, since the heavy ions bring with them

large amounts of momentum, and the target nuclei are rela-
tively light. It is, however, well understood and does not
introduce any dispersion into the data. The laboratory
energies were transformed to center-of-mass energies by the
method described in detail by Haines,[23] which is an itera-
tive procedure with accuracy to 0.02 MeV.

E. Transformations

The primary data may be viewed as a density distri-
bution of events in a pulse-height 1 versus pulse-height 2
plane. By means of a suitable pulse-height energy cali-
bration, the units of this distribution may be changed from
pulse-heights to lab energies. By means of a center-of-
mass (c.m.) computation (Section III-D), and a random number
technique,[4,24] the lab energy density distribution can be
transformed to a c.m. energy distribution. For reasons of
familiarity, and for the purpose of comparing with theory,
yet another transformation has been made. This transformed
the two c.m. energy coordinates to a mass versus total kinetic
energy (E_T^*) coordinate system in the following way. From
the conservation of linear momentum, we have, for any fission
event

$$\frac{A_2}{A_1} = \frac{E_1}{E_2} \quad , \qquad \text{(III-4)}$$

where A is the fragment mass, E the fragment kinetic energy,
and the subscripts refer to the two fragments.

Equation (III-4) is equivalent to

$$\frac{A_1}{A_c} = \frac{E_2}{E_T} \qquad \text{(III-5)}$$

where A_c is the mass of the compound nucleus, and E_T is

the total kinetic energy released in that event $(E_1 + E_2)$.

Thus, if E_1 and E_2 are measured, A_1 can be calculated. This

makes it possible to present the data in terms of a probability

of observing an event with mass A_1 and total kinetic energy

release E_T. Equation (III-5) strictly holds only for

energies before neutron emission, while those measured are

energies after neutron emission.

Thus using E^* to refer to energies uncorrected for

neutron effects, Eq. (III-5) becomes

$$\frac{A_1}{A_c} \approx \frac{E_2^*}{E_T^*} \quad .$$

Since the uncorrected energies appear as a ratio, the error

introduced by replacing E_2/E_T with E_2^*/E_T^* is very small. The

magnitude of the error is discussed in Appendix C. A random

number technique[24,25] was used to transform data from density

distributions in the pulse-height plane to density distri-

butions in the A_1 versus E_T^* plane.

F. Addition of Data

For experimental reasons it was found necessary to

add together data of one type but from different experiments

(see Section II-E). This was done after all corrections

were applied to each file of data separately, and only when

the data were in final two-dimensional form. (The term

"two-dimensional" will henceforth be used to describe data
in the form of a density-of-events distribution in a mass
versus total kinetic energy plane.) The differences between
two distributions of the same type were very small, and were
noticeable only when the average total kinetic energy was
considered. Even in extreme cases the difference was never
larger than 1.2 MeV, and the dispersion introduced into the
final two-dimensional distributions was estimated to be of
the order of a few percent.

G. Statistical Calculations

Use of statistical moments has been made in the
final presentation of the data. First and second moments
have been calculated for the overall distribution in one
independent variable (e.g. mass-yield curves), as well as
for the distribution in one independent variable taken as
a function of the other variable (e.g. mass-yield curves
for a set of E_T values.)

The first moment, μ_1, of a distribution in a variable
x is the mean, $\langle x \rangle$. The second moment, μ_2, is the variance
which is a measure of the width of a distribution

$$\mu_2(x) = \langle x^2 \rangle - \langle x \rangle^2 \quad .$$

(The full width at half maximum, FWHM, is given, for a
Gaussian distribution, by

$$\text{FWHM} = 2.36 \sqrt{\mu_2} \quad .)$$

Higher moments μ_3 and μ_4 were also calculated, but their use was found to be limited due to an insufficient number of events and their high sensitivity to both statistical and systematic errors. The fourth moment, μ_4, was used in estimating statistical standard errors, ϵ_2, in the second moments.[4]

$$\epsilon_2 = (\mu_4 - \mu_2^2)/N_T$$

The error in the first moment, ϵ_1, is given by

$$\epsilon_1 = \sqrt{\mu_2}/N_T \quad ,$$

where N_T is the total number of events.

In spite of the fact that a relatively small number of events was measured in most of the reactions studied, the data were not "folded", i.e. symmetry of mass distributions has not been forced. Although in doing this we forego the advantage of "doubling" the number of events for statistical purposes, we retain valuable checks on the data. The necessary symmetry properties that the two-dimensional distributions have to satisfy have been discussed in the appendix of reference 4. The data presented in this work were found to satisfy all the conditions.

H. Effects of Pre-Fission Neutron Emission

The following effects need to be considered. Each neutron evaporated reduces the excitation energy of the compound nucleus. Since nuclear temperature for purposes

of comparison with theory is calculated from the excitation energy, the average number of neutrons evaporated from the compound nucleus before fission must be known.

In order to estimate the number of neutrons evaporated from the fragments (see Appendix B), energy balance arguments are used. For these considerations, knowledge of the excitation energy at fission is again needed.

Thus even though the number of neutrons emitted before fission does not directly enter into the data processing, it is an important quantity and essential to the interpretation of this work. Theoretical calculations on the competing processes in the decay of the compound nucleus based on cross section measurements are presented in Section IV-D. The problem is discussed fully in that section, and results are tabulated there.

I. Effects of Post-Fission Neutron Emission

The evaporation of neutrons from fission fragments introduces an important dispersion into the two-dimensional data. It is introduced in the following way: each fragment having a definite excitation energy has associated with it a probability distribution, $P(\nu)$, in the number of neutrons that it emits. This $P(\nu)$ distribution has a characteristic width and average value for any given fragment. It arises from the fact that for any fission event having a definite

total kinetic energy, E_T, and mass, A_1, the excitation energy must be shared between the two fragments. There is a distribution that describes the way in which this excitation energy is shared between the two fragments, and therefore, a distribution $P(\nu)$ in the number of neutrons emitted from a given fragment results. At this stage the distribution $P(\nu)$ is not available for these reactions from experimental results, and it cannot be calculated with great confidence. Thus we content ourselves to correct the measured energies only for the average case. An error in this procedure is further introduced in the assumption that has to be made as to how the excitation energy is shared by the two fragments.

Haines[5] and Burnett[4] have derived expressions for the corrections for neutron effects to the average total kinetic energy, $\langle E_T \rangle$, the variance of the total kinetic energy distribution, $\mu_2(E_T)$, and the variance of the mass distribution, $\mu_2(A_1)$. The $\langle E_T \rangle$ and $\mu_2(E_T)$ formulae have been worked out for a given mass. These quantities are therefore a function of mass. $\mu_2(A_1)$ is a function of E_T. The variables in the parentheses are the variables over which the averaging is done. The formulae derived by Burnett have been used in this work. They are based on the assumption, shown above not to be rigorously true, that there is no correlation between the number of neutrons from a given fragment, ν_1, and the fragment mass or total kinetic energy. (i.e.

$\nu_1 = \nu_2 = \nu_T/2$, where ν_T is the total number of neutrons emitted. Its evaluation is discussed in Appendix B.) An outline of the derivation of the expressions is given in the appendix of reference 4. They are also listed in Appendix F of this work.

The most important correction is that made to the total kinetic energy. For a symmetric event, we have

$$\langle E_T \rangle \cong E_T^* \left[1 + \frac{\nu_T}{A_c} \right] \quad ,$$

where the star denotes the uncorrected quantity. This becomes, for the general case,

$$\langle E_T \rangle \cong E_T^* \left[1 + \frac{\nu_T}{2A_c} \left(\frac{A_1}{A_2} + \frac{A_2}{A_1} \right) \right] \quad . \qquad (III-6)$$

A_c is the mass of the compound nucleus, and the subscripts 1 and 2 denote the two fragments. For the overall distributions, $\langle E_T \rangle - \langle E_T^* \rangle$ ranged from 4.5 MeV to 6 MeV for the Os^{186} case and from 4 to 7.5 MeV for the O^{16} bombardments of W^{182}. This large effect, together with the large effect on $\langle E_T \rangle$ of the choice of calibration scheme gave an estimated uncertainty in $\langle E_T \rangle$ of ± 6 MeV, which is 2 MeV higher than the error estimated in the work of Burnett.[4]

The effects of neutrons on the masses calculated in Section III-E is small and has been discussed fully in Appendix C. It is shown that there is an appreciable error in the calculated mass only when the assumption of $\nu_1 = \nu_2 = \nu_T/2$ is very poor. (Even in such a case, the error is only

of the order of two or three mass units.)

The effect of neutrons on the variances has been discussed by Burnett.[4] This effect is remarkably small. Thus it consists in the first approximation of a slight downward shift of the experimental $\mu_2(E_T)$ versus mass curves and of no visible effect on the $\mu_2(A_1)$ versus E_T curves (see Section V). The effect on the widths of the overall distributions (the mass-yield curves and the E_T-yield curves) was somewhat larger. Thus the overall $\mu_2(E_T^*)$ was 154 $(MeV)^2$ for the O^{16} bombardment of W^{182} at 165 MeV, and this was reduced to $\mu_2(E_T) = 131$ $(MeV)^2$ when the neutron correction was applied.

Only neutron corrected results will be presented in this work.

IV. THEORETICAL CONSIDERATIONS

The primary objective of this work is to compare experimental results with those calculated by means of a model developed by Nix.[3] This model is itself an approximation to the liquid drop model, which considers the nucleus to be a homogeneous uniformly charged liquid drop. Nix has been able to calculate theoretical two-dimensional probability distributions, which can be compared directly to the experimental two-dimensional density-of-events distributions obtained here. Both the theoretical and the experimental distributions can be expressed in the mass-total kinetic energy plane, the only difference between the two being that the experimental distribution is obtained after the emission of neutrons, while the model of Nix gives the distributions prior to the emission of neutrons. For the sake of completeness, a summary of the main features of this model will be given in Part C of this section.

An important variable in the model of Nix is the nuclear temperature of the fissioning nucleus in its saddle configuration. The evaluation of this quantity raised considerable difficulties. It is known that at such high excitation energies as are encountered in this work, neutron emission from the compound nuclei is an important process. It may compete with fission in such a way as to allow the nucleus to fission at any point in the chain of successive

neutron emission, thus making the average excitation energy at fission a very ill-defined quantity. Calculations are presented in Part D of this section in which the competition between fission and neutron emission is followed through the evaporation chain. These calculations involve the evaluation of the fission width, Γ_f, for which a knowledge of the fission barrier is needed.

In the case of systems with high angular momentum, the fission barrier is expected to decrease appreciably with increasing angular momentum.[29,30] This effect is important and must be considered in evaluating Γ_f values. Calculations have, therefore, been performed[31] to evaluate the barriers for the rotating liquid drop model. These calculations are presented in Part B of this section. They are an extension of the work of Cohen and Swiatecki.[2]

Part A of this section is devoted to definitions of energy terms. Such familiar terms as "fission barrier", "excitation energy", and "rotational energy" will be defined for the purpose of this work, and will be used throughout the rest of it. The different meanings that various authors attach to these concepts, and the confusion that seems to exist whenever a fissioning rotating nucleus is considered justify a clear definition of terms.

The organization of this section is therefore as follows: After defining in Part A the various terms used,

the statics (or gyrostatics to be exact) of the nucleus is
considered in Part B, resulting in evaluations of the deforma-
tion energies of rotating charged drops. Dynamics is then
considered; a summary of the work of Nix is given in Part C.
Finally, the decay of the compound nucleus is considered in
Part D.

A. Definitions

Consider the case of a nonrotating compound nucleus
(right-hand section of Fig. IV-1). From ground state masses
and bombarding conditions, E_x, the excitation of the compound
nucleus can be calculated. The excitation energy is based
on the ground state mass of the compound nucleus. The
ground state calculated on the liquid drop model (liquid drop
ground state) may lie above or below the true ground state.
(The liquid drop model here is understood to include the odd-
even correction.) The energy separation between the two
ground states is Δ and will be referred to as the "shell
correction". B_f is the true fission barrier for this nucleus,
and B_f^{LD} is the barrier calculated from the liquid drop model.
The fission barrier, B_f, is the difference in energy between
the ground state and the saddle point shape. For the purpose
of this illustration, no shell corrections is indicated at
the saddle. E_x^{saddle} is the excitation energy of the nucleus
in its saddle configuration.
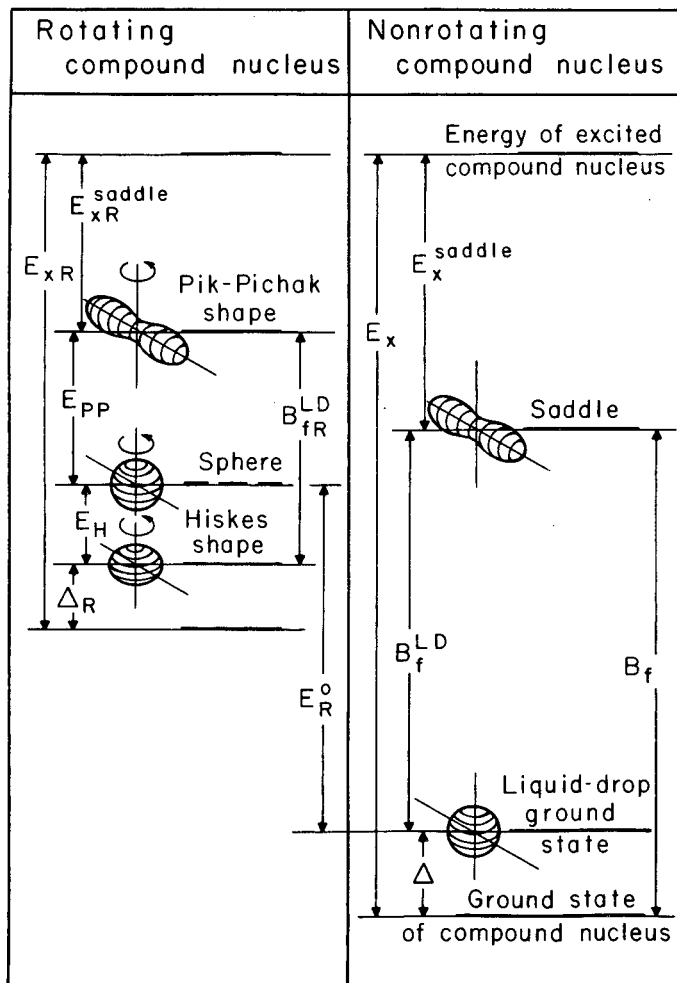
MU-33158

Figure IV-1.   This figure defines the energy terms used in this
work. It is a schematic and the absolute magnitude
of the spacing of energy levels shown here has no
physical significance. The various energies are
described in the text. Subscript R stands for
rotation, subscript x for excitation, subscript H
for Hiskes shape, subscript PP for Pik-Pichak shape,
B_f is used to denote the fission barrier, Δ is the
shell correction. The superscript LD stands for
the liquid drop model, superscript "saddle" for
excitation energies of saddle point shapes, and the
superscript o for the spherical nucleus.

$$E_x^{saddle} = E_x - B_f$$

Now consider a rotating compound nucleus. Subscripts R are applied in all cases where needed to distinguish the terms from the nonrotating case. If the nucleus were not allowed to deform, and were forced to remain spherical, its rotational energy, E_R^O, could easily be calculated from the angular momentum of the system. Thus E_R^O is given by

$$E_R^O = \frac{L^2}{2\mathcal{J}_O} \qquad (IV-1)$$

where L is the angular momentum, and $\mathcal{J}_O$ is the rigid body moment of inertia. (The use of the rigid body moment of inertia at such high excitation energies as are encountered here is suggested by reference 49.) This rotational energy, E_R^O, is indicated in the left section of Fig. IV-1. The rotating compound nucleus, however, deforms to an equilibrium position of lower energy than the sphere (see Part B of this section). This shape has been called the Hiskes shape.[30] It lies at an energy E_H below the spherical shape. The Hiskes shape calculated on a liquid drop model neglects all shell corrections, and the true equilibrium state may be removed from it by an energy of Δ_R in analogy with the nonrotating case. If the rotating saddle-point configuration referred to as the Pik-Pichak shape is at an energy E_{PP} (Pik-Pichak energy) above that of the rotating sphere, the barrier according to the liquid drop model is given by

$$B_{fR}^{LD} = E_{PP} + E_H \quad .$$

The true fission barrier includes the shell correction and is given by

$$B_{fR} = E_{PP} + E_H + \Delta_R \quad . \qquad (\text{IV-2})$$

The excitation energy, E_{xR}, (excluding the "unavailable" rotational energy) of the stable equilibrium shape of the rotating compound nucleus is given by

$$E_{xR} = E_x - E_R^O + E_H - \Delta + \Delta_R \quad . \qquad (\text{IV-3})$$

For the extreme case of equal shell correction in the rotating and nonrotating nucleii, $\Delta = \Delta_R$, and the above equation reduces to

$$E_{xR} = E_x - E_R^O + E_H \quad . \qquad (\text{IV-4})$$

For the other extreme of no shell effects in the rotating case, $\Delta_R = 0$; the equation becomes

$$E_{xR} = E_x - E_R^O + E_H - \Delta \quad . \qquad (\text{IV-5})$$

The expression for E_{xR}^{saddle}, the excitation energy in the rotating saddle configuration, is:

$$E_{xR}^{saddle} = E_x - E_R^O - E_{PP} - \Delta \quad . \qquad (\text{IV-6})$$

Certain terms in common usage in liquid drop calculations will be used in this section. If E_c^O and E_s^O are the Coulomb and surface energies of a spherical nucleus, respectively, we may define the fissionability parameter, x, by

$$x = E_c^O / 2E_s^O \quad ,$$

and the rotational parameter, y, by

$$y = E_R^O / E_S^O \quad .$$

(The superscripts, ^{O}, refer to spherical shapes.)

For any given shape the deformation energy (in units of E_S^O) is defined by

$$\xi = \frac{E_c + E_s + E_R - E_c^O - E_s^O - E_R^O}{E_s^O}$$

$$= \frac{E_{total} - E_{total}^O}{E_s^O}$$

The subscripts c, s, and R denote Coulomb, surface and rotational energies respectively.

B. Deformation Energy of a Uniformly Charged Rotating Liquid Drop[33]

1. Method of Calculation

The method used is a simple extension of the method used in reference 2. The shape of the deformed nucleus is described by an expansion in Legendre polynomials. The radius vector, $R(\theta)$, is given by

$$R(\theta) = \frac{R_o}{\lambda} \left[1 + \sum_{n=1}^{n=18} \alpha_n P_n(\cos \theta) \right] \quad ,$$

where $R(\theta)$ and θ are defined in Fig. IV-7, λ is a volume normalization constant, $P_n(\cos \theta)$ is a Legendre polynomial of order n, α_n's are coefficients of the expansion, and R_o is the radius of the spherical drop. The use of Legendre polynomials restricts the shapes to axial symmetry. This restriction introduces an approximation which is discussed later.

An additional disruptive force, the rotational energy E_R, was added to the surface and Coulomb energies. It is given by

$$E_R = \frac{L^2}{2\mathcal{J}} \quad ,$$

where L is the angular momentum, and $\mathcal{J}$ is the rigid body moment of inertia of the drop about the vertical axis in Fig. IV-7. The IBM-7090 FORTRAN program of reference 2 was extended to include the rotational energy.

Since three energies are considered in this model $(E_s, E_c,$ and $E_R)$, two dimensionless ratios in terms of which all results may be discussed are required. These were chosen to be the fissionability parameter, x, and the rotational parameter, y, both defined in Part A of this section.

2. Qualitative Results

Two sequences of equilibrium shapes have been calculated in this work: the shapes of stable equilibrium, and the shapes of unstable equilibrium.

The sequence of stable equilibrium shapes starts out with a spherical nucleus (for a system with no rotation) and describes the deformations of the nucleus as the amount of rotation increases. The sequence of unstable equilibrium shapes represents saddle-point configurations associated with the barrier for the disintegration of the system. Thus for no rotation the shape of unstable equilibrium is simply the saddle configuration of Cohen and Swiatecki.[2]

Starting with a spherical nonrotating nucleus, the sequence of stable equilibrium shapes, as y (the amount of rotation) increases, is as follows:

For a small amount of rotational energy, the sphere flattens into an oblate spheroid at all values of x. (For large amounts of rotational energy, the shape is no longer an exact spheroid. It will be referred to as a pseudo-spheroid.) These spheroids and pseudospheroids have been called Hiskes shapes.[30,41] As the rotational energy increases, the centrifugal force continues to flatten the pseudo-spheroid further, until a critical value of y is reached, at which the Hiskes shape undergoes a qualitative transition. The critical value of y at which the transition takes place is a function of x. It is shown in the y versus x plot of Fig. IV-4 by the lower line. The nature of the transition depends on whether x is above or below a certain critical value x_c. If x is greater than x_c, the barrier for the disintegration of the system vanishes, and the drop is unable to support further rotation. If x is less than x_c, further rotation changes the shape of the nucleus to a pseudo-ellipsoid, which has ellipsoidal symmetry and three unequal axes. This elongated figure, referred to as the Beringer-Knox shape,[33,42] is rotating about its shortest axis. The elongation of the pseudoellipsoid increases when the rotational energy is increased further, until it reaches a

second critical value of y, at which it follows the same
fate as the Hiskes shape did for $x > x_c$. Unable to support
further rotation, it disintegrates. This second critical
value of y (again a function of x) is denoted by the top
curve of Fig. IV-4. The top and bottom curves of Fig. IV-4
should merge at $x = x_c$. This appears to be at x=0.7 in
the y versus x plot of Fig. IV-4. The value of x_c, however,
is believed to be between x=0.81 and x=0.825.[34,35] This
apparent discrepancy is discussed in Subsection IV-B-3.

Thus the sequence of stable equilibrium shapes is
as follows: $x < x_c$

sphere———→pseudospheroid———→pseudoellipsoid———→disintegration
for $x > x_c$

sphere———→pseudospheroid———→disintegration

Considering the unstable equilibrium sequence, the
important feature is the decrease of the saddle point
deformation energy as the drop is rotated. This decrease
continues with increasing rotation, until the barrier for
disintegration disappears, the stable and unstable equili-
brium shapes merge together, and no further equilibrium
shapes exist. (The upper limit in Diagram IV-4). In the
case of necked-in saddle point shapes, the neck tends to fill
in as rotation is increased. At the same time the shape tends
to deviate from axial symmetry with increasing rotation. The
name of Pik-Pichak shapes has been suggested for the rotating

saddle point configurations.[29,33]

In Fig. IV-2 the deformation energy is plotted as a function of y for x=0.54 (i.e. for x well below x_c). The points on the graph are points at which the calculation was carried out. The solid lines were drawn so as to connect the calculated points. The closed circles represent the Pik-Pichak family of equilibrium shapes and the open circles the Hiskes family. At y ≈ 0.107, the first critical value of y is reached, and the pseudoellipsoid (closed triangles) becomes more stable than the pseudospheroid. At y ≈ 0.152, the curves for the pseudoellipsoids and the saddle point shapes merge, and no stable configurations with greater rotation exist.

The difference in energy between the Pik-Pichak shapes and either the Hiskes shape or the Beringer-Knox shape (whichever is more stable) is the fission barrier, B_{fR}^{LD}.

3. Approximation and Corrections

The only approximation in this work is the imposed axial symmetry on the Pik-Pichak and Beringer-Knox shapes. This results from the choice of Legendre polynomials to describe the shape of the nucleus. For very elongated shapes, this approximation is good, but for shapes which have three widely differing axes, it is very poor. In this region where our approximation does not hold, however, the ellipsoidal

x = 0.54

● Pik-Pichak shapes
○ Hiskes shapes
▲ Beringer-Knox shapes
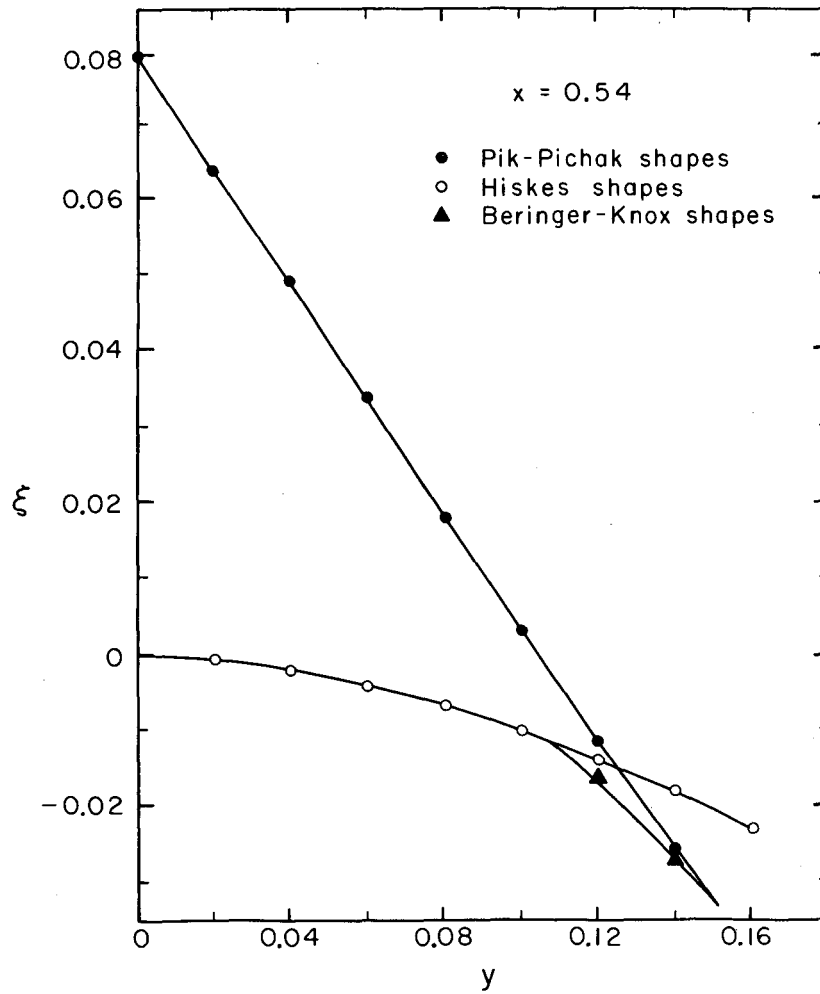
MU-33159

Figure IV-2. The deformation energies for the three families of equilibrium shapes for x=0.54 as a function of rotational parameter y. Points at which the energies were calculated are shown by the circles and triangles. Solid lines were drawn through the calculated points. The lines for Beringer-Knox shapes and Pik-Pichak shapes approach each other quadratically.

approximation used by other authors[35,38] is good, and the two
results may be combined to possibly give a fairly correct
overall picture. This will be done in greater detail in
another paper.[37]

The lower solid line in Fig. IV-4 between $x=0.5$ and
$x=0.62$ is obtained from our calculations. It corresponds
for any given y to the point where the pseudoellipsoids in
our calculation become more stable than the pseudospheroids.
The open circles in Fig. IV-4 were deduced from the calcula-
tion of Carlson.[38] Good agreement between Carlson's results
and ours was found up to about $x=0.62$. Beyond this point,
the disagreement is thought to be due to the inaccuracy of
our code in evaluating the triaxial Beringer-Knox shapes.
For x values greater than 0.62, no pseudoellipsoids of greater
stability than pseudospheroids were obtained by our method,
even though the x value is well below x_c. The deformation
energies for $x=0.68$ shown in Fig. IV-3 illustrate this point.

When the line drawn through the Hiskes energies in
Fig. IV-3 is allowed to approach quadratically the line passing
through the Pik-Pichak shapes, an estimate of the point at
which the barrier to fission vanishes is obtained. (The use
of quadratic merging of the two families of shapes is
suggested by the work of Cohen and Swiatecki.[36]) This pro-
cedure was used for $x > 0.62$ to obtain the upper curve of
Fig. IV-4. This curve was found to coalesce for practical
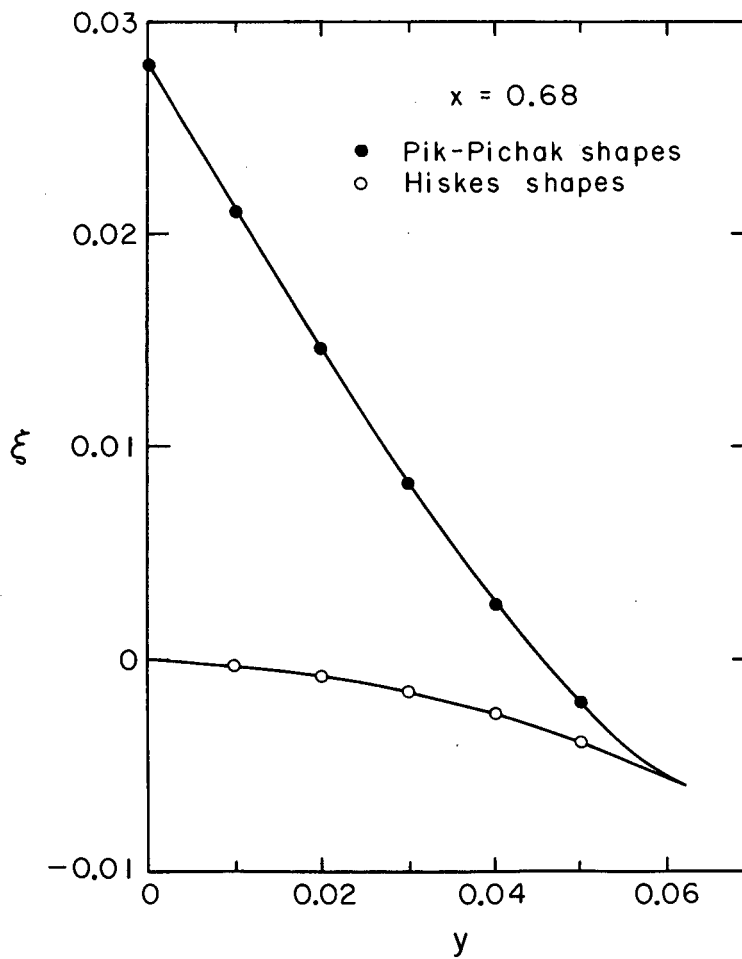
Figure IV-3. Deformation energies of equilibrium shapes for x=0.68. The Beringer-Knox pseudoellipsoids have disappeared.
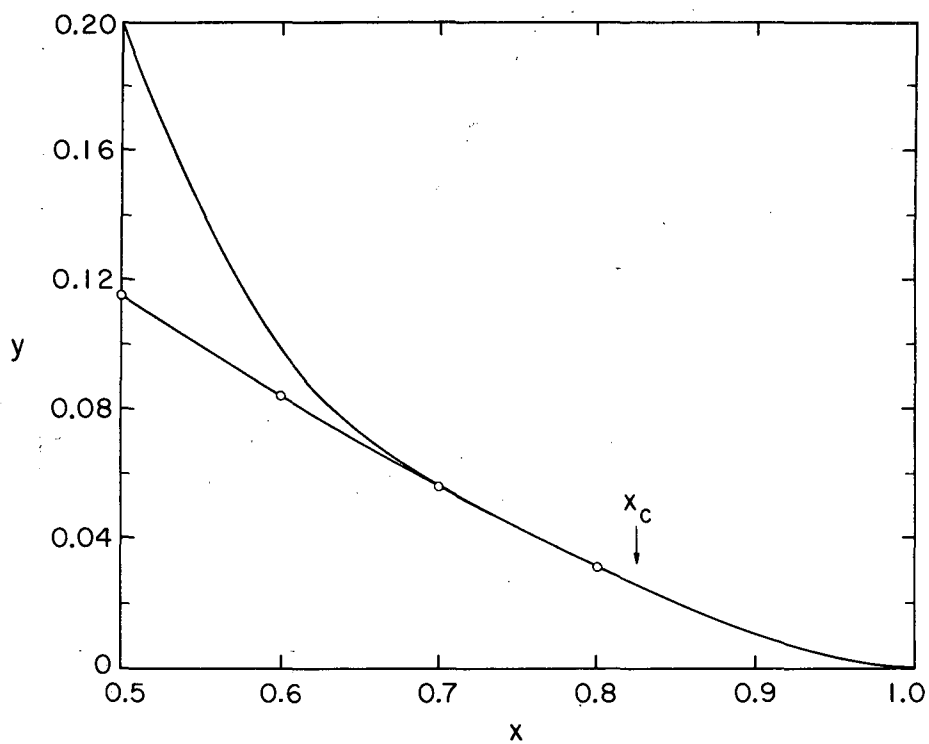
Figure IV-4.   Illustration of the regions of x and y in which
                various equilibrium shapes exist. Below the lower
                curve, Hiskes pseudospheroids are the stable
                equilibrium shapes. Between the lower and the
                upper curves, the stable equilibrium configura-
                tion takes the shape of Beringer-Knox pseudo-
                spheroids. Above the upper curve no equilibrium
                shapes exist. The open circles are points from
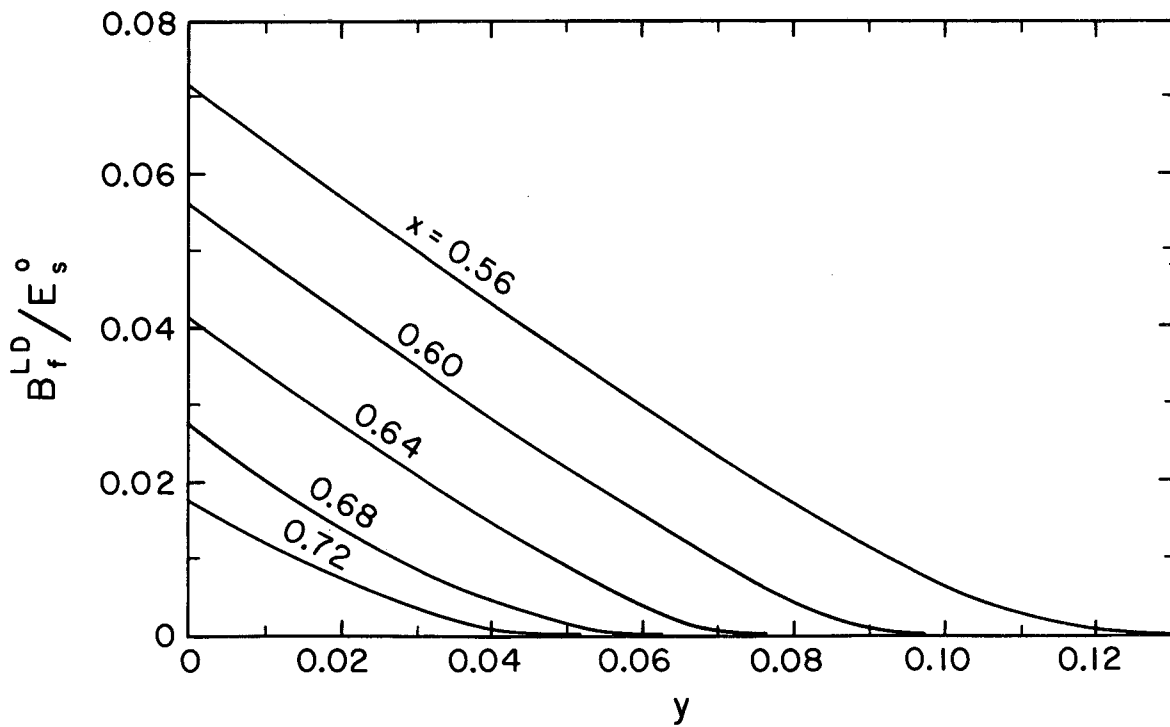   the work of Carlson.[38]

purposes with the lower one (which was calculated beyond

x ≃ 0.62 by Carlson's method) at about x=0.7. This seems

to indicate a negligible region of Beringer-Knox shapes

from x=0.7 to x_c and a very small region of Beringer-Knox

shapes from x ≃ 0.62 to x=0.7.

Barriers given in the following subsection for x

values above 0.62 are differences in energy between the

Pik-Pichak shapes and Hiskes shapes (i.e. between the two

lines of Fig. IV-3). Beringer-Knox shapes in this region

have been neglected. The error thus introduced into the

barriers becomes appreciable percentage-wise only for very

small values of the barriers. In such a case, however, the

absolute magnitude of the barrier makes the errors unimpor-

tant for the purpose of this work.

4. Quantitative Results

The results presented here cover only the region of

x values of interest in this work. A complete tabulation

will be given in another paper.[37] Fig. IV-5 shows the

fission barrier B_f^{LD} (in units of E_s^o) for a set of x values.

The rapid decrease of the barriers with increasing y has

important consequences for this work. It makes it necessary

to consider B_f^{LD} as a function of the angular momentum when

evaluating E_{xR}^{saddle} .

Figure IV-6 gives B_f^{LD} as a function of x. The line

for y=0 is the same as that evaluated by Cohen and Swiatecki.[2]

Figure IV-5. Fission barrier B_f^{LD} in units of the surface energy of the sphere, as a function of y for different x values.

B_f^{LD}/E_s^o

$y = 0$
0.01
0.02
0.03
0.04
0.05
0.06
0.07
0.08

X
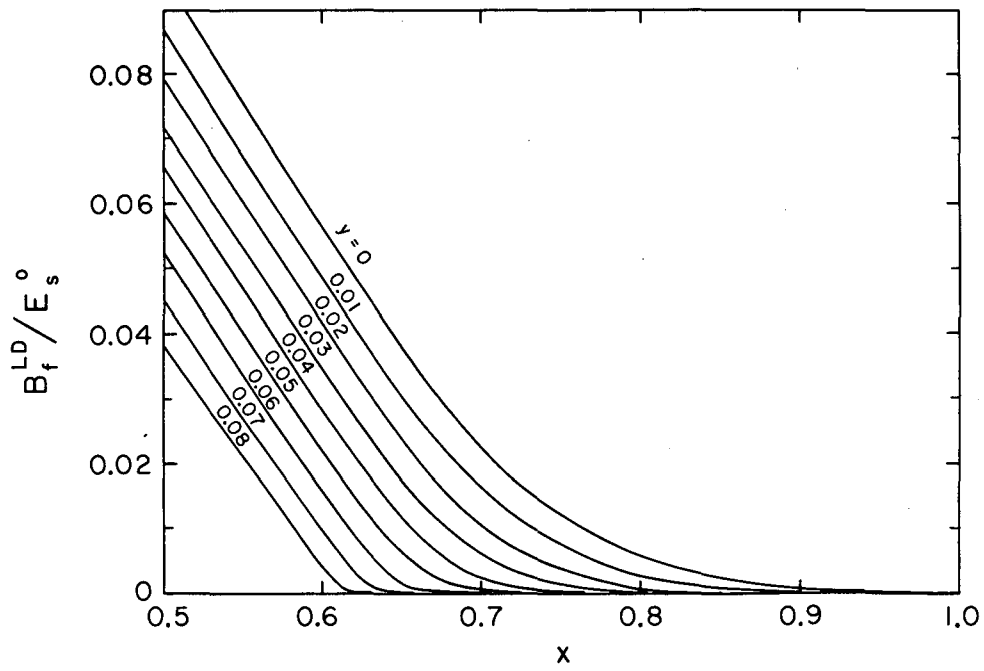
MU-33163

Figure IV-6. Fission barriers as a function of x for different y values.

Table IV-1 gives ξ_{PP}, the deformation energy of the Pik-Pichak shape in units of E_s^o, and Table IV-2 gives ξ_H, the deformation energy of the Hiskes shape. Data in these tables were used in calculations of Section IV-D for the evaluation of E_{xR} and E_{xR}^{saddle}.

5. <u>Summary of the Liquid Drop Calculations</u>

These calculations have been performed to obtain energy values to be used in the Γ_f evaluation (Section IV-D), which in turn is needed for obtaining the average excitation energy at fission. The steps in the calculation were the following:

(a) Modification of the code of Cohen and Swiatecki[2] to include rotational energies.

(b) Evaluation of equilibrium configurations (stable and unstable) using the modified code.

(c) Determination of the region in the x-y diagram in which Beringer-Knox pseudoellipsoids are more stable than Hiskes pseudospheroids, and comparing results to those of Carlson.[38]

(d) Determination of the limit in the amount of rotation that the drop can support. This was done by allowing the deformation energies, ξ_H and ξ_{PP} to approach each other quadratically for $x > 0.62$, and by allowing $\xi_{Beringer-Knox}$ to approach ξ_{PP} quadratically below $x=0.62$.

(e) Construction of curves of B_{fR}^{LD} as a function of x and

Table IV-1. Deformation energy of the unstable equilibrium shape ξ_{PP} in units of E_s^o as a function of fissionability parameter, x, and the rotational parameter, y.

y	x=0.58	x=0.60	x=0.62	x=0.64	x=0.66	x=0.68	x=0.70	x=0.72	x=0.74	x=0.76
0	0.06396	0.05636	0.04886	0.04154	0.03451	0.02798	0.02230	0.01757	0.01369	0.01053
.01	0.05636	0.04880	0.04137	0.03415	0.02729	0.02113	0.01599	0.01185	0.00855	0.00594
.02	0.04878	0.04126	0.03390	0.02681	0.02022	0.01456	0.01006	0.00658	0.00393	0.00197
.03	0.04122	0.03375	0.02648	0.01956	0.01336	0.00837	0.00463	0.00192	0.00006	-0.00106
.04	0.03367	0.02627	0.01912	0.01246	0.00684	0.00271	-0.00009	-0.00176	–	–
.05	0.02614	0.01883	0.01184	0.00558	0.00086	-0.00210	-0.00350	-0.00475	–	–
.06	0.01865	0.01144	0.00469	-0.00084	-0.00410	-0.00510	–	–	–	–
.07	0.01263	0.00413	-0.00220	-0.00630	–	–	–	–	–	–
.08	0.00377	-0.00310	-0.00700	–	–	–	–	–	–	–

Table IV-2. Deformation energy of the stable equilibrium shape ξ_H in units of E_S^0 as a function of the fissionability parameter, x, and the rotational parameter, y.

y	x=0.58	x=0.60	x=0.62	x=0.64	x=0.66	x=0.68	x=0.70	x=0.72	x=0.74	x=0.76
0	0.	0.	0.	0.	0.	0.	0.	0.	-0.	-0.
.01	-0.00015	-0.00016	-0.00017	-0.00017	-0.00018	-0.00019	-0.00020	-0.00022	-0.00023	-0.00025
.02	-0.00055	-0.00058	-0.00060	-0.00066	-0.00066	-0.00070	-0.00074	-0.00078	-0.00083	-0.00088
.03	-0.00119	-0.00124	-0.00129	-0.00135	-0.00141	-0.00148	-0.00156	-0.00164	-0.00174	-0.00184
.04	-0.00203	-0.00211	-0.00220	-0.00230	-0.00240	-0.00251	-0.00263	-0.00277	–	–
.05	-0.00307	-0.00319	-0.00331	-0.00345	-0.00359	-0.00375	-0.00400	-0.00485	–	–
.06	-0.00428	-0.00444	-0.00461	-0.00479	-0.00498	-0.00519	–	–	–	–
.07	-0.00565	-0.00585	-0.00607	-0.00630	–	–	–	–	–	–
.08	-0.00717	-0.00742	-0.00769	–	–	–	–	–	–	–

y. B_{fR}^{LD} values were obtained from $\mathcal{E}_{PP} - \mathcal{E}_H$ for x > 0.62

and from $\mathcal{E}_{PP} - \mathcal{E}_{Beringer-Knox}$ below x=0.62, whenever the

Beringer-Knox shape was more stable than the Hiskes shape.

(f) Tabulation of $\mathcal{E}_H$ and $\mathcal{E}_{PP}$ for use in calculation of

Section IV-D.

C. The Spheroid Model of Nix[3,39]

The calculation of the deformation energies of

distorted liquid drops of Cohen and Swiatecki[2] shows that

the saddle-point shapes resemble elongated dumbbells with

a pronounced neck in the region of x between x=0 and about

x=0.67. Above x=0.67 the neck disappears, and the drop

contracts until it becomes a sphere at x=1. The existence

of a neck in the saddle configuration suggests that the

fate of the scissioning drop is determined by its configura-

tion at the time of its passage over the saddle. Calcula-

tions involving the dynamics of the liquid drop as it passes

over the saddle could yield results that would lend them-

selves to comparisons with experimental data. Such calcula-

tions would have been very difficult to carry out in the

usual Legendre-polynomial parametrization of the liquid drop.

Nix has chosen to approximate the fissioning system by two

spheroids, which can be either overlapping, tangent to each

other, or separated. His parametrization of the drop is

shown in the lower part of Fig. IV-7. The coordinates involved

are the following: the two semi-major axes c_1 and c_2, the
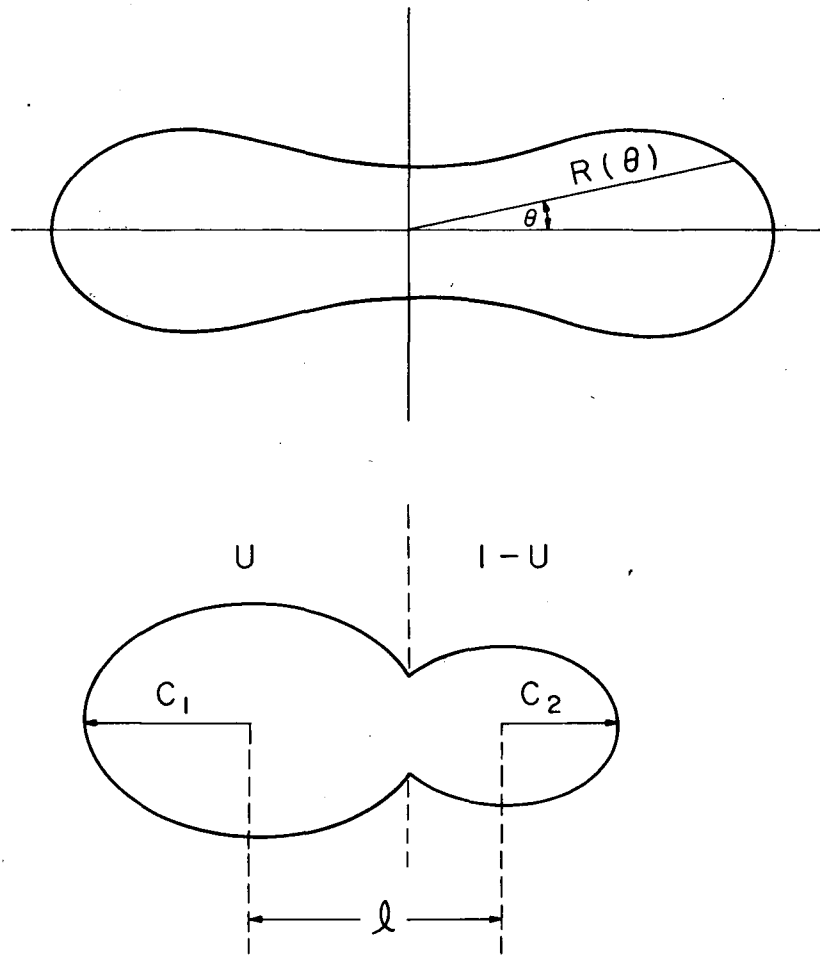
MU-33164

Figure IV-7. Parameters used in describing the shape of liquid
drops. The top figure gives the parameters used
in the expansion of Legendre polynominals. The
bottom figure gives the parameters used by Nix
in the spheroid model.

separation coordinate ℓ, and the asymmetry coordinate U.

Nix has evaluated the energies of deformation for his model. He found that the saddle-point configurations consisted of symmetric tangent spheroids up to x ≈ 0.8. These gave way to overlapping spheroids for higher values of x. Thus the qualitative features of the liquid drop model as worked out by Cohen and Swiatecki[2] are reproduced by the spheroid model in the region of x values below x ≈ 0.67, and again for x values above x ≈ 0.8. Most of the experimental fission data lie in the region between x=0.67 and x=0.8, where this model is not expected to apply. The x values for the reactions studied here, however, are approximately 0.62 and 0.67, i.e. within the region where the model is expected to give good results.

The calculations may be outlined as follows:

The first step involved is the evaluation of the potential energy of the system. This step is similar to the work of Cohen and Swiatecki[2] and gives saddle-point shapes and energies.

The second step concerns the evaluation of the kinetic energy of the system and the solution of classical equations of motion. At this point, given a liquid drop in an initial state of motion, its energy and deformation may be followed through the scission and fragment separation processes to infinity.

In the third step the distribution of initial condi-

tions at the saddle is determined by transforming to normal coordinates and assuming statistical equilibrium. In calculating the vibrational motion in the neighborhood of the saddle point, it was possible to obtain solutions that were correct quantum mechanically, as well as classically. This step results in a Gaussian probability distribution for each normal coordinate and its conjugate momentum, with a temperature-dependent width.

In the last step the distributions in initial conditions and the relationship between these conditions and the kinetic energy were combined to obtain the probability $N(E_T, A_1)$ of observing a given fragment total kinetic energy E_T and mass A_1.

Appendix D gives the approximate expression of Nix for $N(E_T, A_1)$. This has been programmed for the LRL 7094 computer by Burnett.[4] The program calculated numerically the overall distribution and moments of the mass and total kinetic energy distributions, using the same grid spacing as those used for the experimental data. Nix has derived approximate analytical expressions, based on the formula of Appendix D, for quantities of interest in this work $(\mu_2(E_T), \mu_2(A_1),$ etc.). The procedure of numerical integration over his complete probability distribution formula, however, has been used here to compare with experimental results.

The remarkable feature of this theory is that a simple model (however crude it may be) has been consistently

followed through the entire fission process. The theory may be directly compared with experiments, and it involves no parameters that can be adjusted during the course of these comparisons. (Constants for the semi-empirical mass formula used in the theoretical calculations have been obtained from Green's analysis of ground state masses and have not been treated as adjustable parameters.)

D. Decay of the Compound Nucleus

To estimate the nuclear temperature of the fissioning nucleus, a knowledge of its excitation energy in the saddle configuration is required. The problem of evaluating this excitation energy is complicated by two factors.

(a) At such high initial excitation energies (up to 130 MeV) as are dealt with here, the competition of neutron emission with fission may be such as to allow the compound nucleus to de-excite by emitting several neutrons, with a large probability for fission at any point in the cascade. This would make the excitation energy at fission, and hence the temperature, uncertain.

(b) During the course of the bombardment, the projectiles strike the target nucleus with varying impact parameters, ranging from zero to the limit of interaction of nuclear forces. Thus, the angular momentum, L, for the system studied ranges from zero to a maximum value L_{max}.

This range of L values implies a range of B_{fR} and in $E_R{}^o$, both of which again tend to make E_{xR}^{saddle} poorly defined.

These two effects have been taken into account in the calculation presented here. Basically these calculations consist of evaluating σ_f/σ_c, where σ_f is the fission cross section, and σ_c is the compound nucleus cross section. The σ_f/σ_c values were fitted to experimental σ_f/σ_R values of Sikkeland and Viola.[28] (σ_R is the total reaction cross section.) Average values of E_{xR}^{saddle} are obtained as a result of these fits. Also obtained for any given reaction are the following quantities: $\langle E_x \rangle$, $\langle \nu_p \rangle$, $\langle L \rangle$, where $\langle \nu_p \rangle$ is the average number of neutrons emitted before fission, $\langle L \rangle$ is the average angular momentum of the fissioning nucleus, and $\langle E_x \rangle$ is the average of the <u>total</u> excitation energy (including rotation) of the compound nucleus prior to its fission.

1. Method of Calculation

Let us define the branching ratio for fission, $\mathcal{G}_f(L)$, in a case of competition of fission with neutron emission for a nucleus of given excitation energy and a given amount of angular momentum, L, by

$$\mathcal{G}_f(L) = \frac{\Gamma_f}{\Gamma_f + \Gamma_n} \tag{IV-7}$$

Γ_f and Γ_n (both functions of L and excitation energy) are the level widths for fission and neutron emission respectively. The branching ratio for neutron emission, $\mathcal{G}_n(L)$, is similarly defined by

$$\mathcal{G}_n(L) = \frac{\Gamma_n}{\Gamma_f + \Gamma_n} \tag{IV-8}$$

Now consider the effect of the neutron evaporation chain. Since excitation energy varies up and down the chain, the branching ratios, $g_f(L)$ and $g_n(L)$, must be evaluated at each stage. Let $g_f^m(L)$ be the branching ratio for fission prior to the evaporation of the m'th neutron from the compound nucleus, and let $g_n^m(L)$ be the corresponding branching ratio for the evaporation of the m'th neutron. Using these definitions, the probability, $P_f^m(L)$ (at a given value of the angular momentum L), for fission prior to the emission of the m'th neutron is given by

$$P_f^m(L) = g_f^m(L) \prod_{i=1}^{i=m-1} g_n^i(L) \quad . \qquad (IV-9)$$

The next step is to consider a nucleus resulting from a heavy ion bombardment. In Appendix E it is shown that the the maximum amount of angular momentum, L_{max}, that the resulting compound nucleus could have, is easily calculable for given bombarding conditions. It is also shown in Appendix E, that the probability of the compound nucleus having an angular momentum between L and L + dL is given classically by $\frac{2LdL}{L_{max}^2}$. Thus to obtain the overall probability, P_f^m, for fission prior to the emission of the m'th neutron, we must integrate the partial probability, $P_f^m(L)$ over the angular momentum distribution. Thus the expression for P_f^m is

$$P_f^m = \int_{L=0}^{L=L_{max}} \frac{2P_f^m(L)LdL}{L_{max}^2} \qquad (IV-10)$$

Neglecting processes other than neutron emission and fission,

we have

$$\frac{\sigma_f}{\sigma_c} = \sum_m P_f^m \quad . \qquad (IV-11)$$

The above assumption implies that whenever a compound nucleus is formed, it will de-excite either by fissioning or by emitting neutrons. The problem of evaluating Γ_n / Γ_f need now be considered. A modified version of the formula given by Huizenga and Vandenbosch[43] has been used:

$$\frac{\Gamma_n}{\Gamma_f} = \frac{4 \, A^{2/3} \, a_f \, E_{xR}'}{K_o a_n \left[2a_f^{\frac{1}{2}}(E_{xR}^{saddle})^{\frac{1}{2}} - 1\right]} \exp\left[2a_n^{\frac{1}{2}}(E_{xR}')^{\frac{1}{2}} - 2a_f^{\frac{1}{2}}(E_{xR}^{saddle})^{\frac{1}{2}}\right].$$

$$(IV-12)$$

A is the mass of the nucleus, K_o is a constant taken to be 11.4 MeV, a_f and a_n are the level density parameters for the fission and neutron emission processes respectively. E_{xR}' is the excitation energy of the nucleus <u>after</u> the neutron (the emission of which we are considering in competition with fission) has been emitted. E_{xR}^{saddle} on the other hand refers to the excitation energy at the saddle before the neutron under consideration is emitted. The dash superscript on E_{xR}' indicates that we are considering the nucleus after neutron evaporation. Thus E_{xR}' is given by a modified version of Eq. (IV-3)

$$E_{xR}' = E_x - E_R^O + E_H' - \Delta + \Delta_R - B_n \quad , \qquad (IV-13)$$

where B_n is the binding energy of the neutron. E_{xR}^{saddle} is given by Eq. (IV-6)

$$E_{xR}^{saddle} = E_x - E_R^O - E_{PP} - \Delta$$

The quantity E_x, when considered somewhere along an evaporation chain, has the following meaning. If E_x^m is E_x prior to the emission of the m'th neutron, it is given by

$$E_x^m = E_x^{\text{original}} - \sum_{i=1}^{i=m-1} (B_n^i + E_n^i + E_{Rn}^i) \quad , (\text{IV-14})$$

where E_x^{original} is simply the E_x as defined in Section IV-A. B_n^i is the binding energy of the i'th neutron, and E_n^i is its kinetic energy. E_{Rn}^i is the rotational energy carried off by the i'th neutron. The value used for E_n is given by $E_n = 2\theta$ where θ is the nuclear temperature, i.e.

$$E_n \cong 2\sqrt{\frac{E_x}{a_n}} \qquad 44 \qquad . \qquad (\text{IV-15})$$

B_n and E_x^{original} have been calculated using Cameron's masses. E_{PP} and E_H were obtained from the tabulations of Section IV-B. Δ has been obtained from the work of Swiatecki,[45] and calculations of rotational energies are given in Appendix E.

The sequence of calculations was as follows:

(a) Rotational parameters (e.g. L_{max}) were evaluated (see Appendix E).

(b) Values of E_x^m were calculated (Eq. IV-14).

(c) Interpolation in Tables IV-1 and IV-2 gave E_H' and E_{PP}.

(d) $\mathcal{G}_f(L)$ and $\mathcal{G}_n(L)$ were evaluated from Eqs. (IV-7), (IV-8), (IV-12).

(e) $P_f^m(L)$ values were obtained from Eq. (IV-9).

(f) P_f^m values were evaluated from Eq. (IV-10) by integration over the angular momentum distributions.

(g) σ_f/σ_c was obtained from Eq. (IV-11).

(h) Averages of E_x, E_{xR}^{saddle}, L, and ν_p were calculated for the fissioning nucleus.

The calculations have been carried out on the LRL 7094 computer. The program was checked by reproduction of the final calculation of reference 46.

2. Results

The ratios σ_f/σ_c calculated as described in the above subsection were compared to the experimental σ_f/σ_R results of Sikkeland and Viola.[28] σ_c and σ_R are different since σ_R includes $\sigma_c$ as well as any noncompound nucleus reactions. In the first attempts to fit our σ_f/σ_c calculations to the experimental data, the difference between σ_c and σ_R was thought to be small. It soon became evident, however, that no matter how much the parameters used in our calculations were allowed to vary, the entire σ_f/σ_R excitation function of Sikkeland and Viola could not be reproduced. The parameters that could be regarded as subject to adjustment in the σ_f/σ_c calculations are the following:

(a) the two nuclear level density parameters, a_f and a_n; (b) the value of $(Z^2/A)_{crit}$ (see footnote 32) in determining x values (and, as a result, in determining E_H and E_{PP}); (c) ΔL_n, the angular momentum carried off by each neutron from the compound nucleus; (d) Δ_R, the shell effect which influences the rotating nucleus in its stable equilibrium. The effect

of varying all of these quantities in turn is shown in Fig.
IV-8, which compares calculations and data for the Er^{170} +
O^{16} case. σ_f/σ_c and σ_f/σ_R are plotted on the same scale.
Table IV-3 gives the parameters for each of the curves. The
heavy curve represents data of Sikkeland and Viola.

Curve I approaches σ_f/σ_R at high energies, but
deviates very rapidly at lower energies. From this and
other attempts, it was concluded, as was found by other
authors[46,49] in similar analyses of fission cross section
data, that when a_n and a_f are taken to be equal, no adequate
fits to the data can be obtained. a_n was therefore decreased
to A/9 and the result is shown in Curve II, which will serve
as a base for examining the effect of other parameters. These
other parameters are now varied one by one: $(Z^2/A)_{crit}$ in
Curve III, Δ_R in Curve IV (for this curve, Δ_R was taken to
be equal to Δ), ΔL_n in Curve V. In Curve VI the absolute
magnitude of a_f and a_n was varied.

The conclusion was that the parameters having the
largest effect on the curves are $(Z^2/A)_{crit}$ and a_n (for fixed
a_f). Furthermore, no parameter introduced any effect that
could be used to reproduce the solid curve of Sikkeland and
Viola. The reason for this is thought to be due to a very
large difference between σ_c and σ_R at higher bombarding
energies. It is known[9,47] that other processes compete with
compound nucleus formation, but their magnitude was not
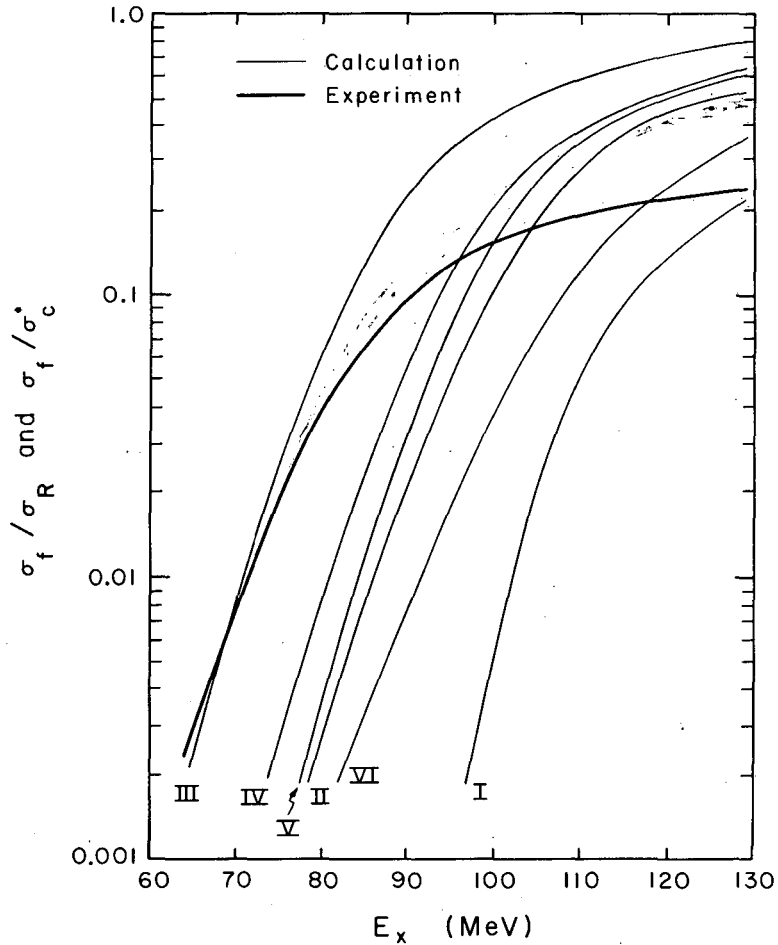
Figure IV-8. Comparison of calculated values of the ratio
σ_f/σ_c (light curves) with the experimental ratio
σ_f/σ_R from the Sikkeland and Viola data for the
reaction $Er^{170}+O^{16}$ (heavy curve). Various
adjustable parameters are changed from one curve
to another. Table IV-3 gives a list of adjust-
able parameters for this figure.

Table IV-3. Values of adjustable quantities used in
curves of Fig. IV-8.

| Curve Number	a_f	a_n	r_o (fermis)	$(Z^2/A)_{crit}$	Δ_R	ΔL_n (units of $\hbar$)
I	A/8	A/8	1.5	50.12	0	2
II	A/8	A/9	1.5	50.12	0	2
III	A/8	A/9	1.5	48.9	0	2
IV	A/8	A/9	1.5	50.12	Δ	2
V	A/8	A/9	1.5	50.12	0	0
VI	A/12	A/13	1.5	50.12	0	2

thought to be large enough to account for the difference
suggested by this analysis. These processes are not due to
breakup as a result of excessive angular momentum discussed
in reference 31, since the angular momenta encountered in
this work are not large enough. Furthermore, the existence
of charged particle evaporation from the compound nucleus,
while not negligible,[47] would not increase the calculated
σ_c by very much if it were included in the calculation. To
suggest an explanation for this apparent discrepancy is
beyond the scope of this work. The factor of importance
here is that fits of calculations to the data are expected
to be better at low excitation energies than at high excita-
tion energies, since reactions are usually simpler and better
understood in this region. Starting at low excitation
energies with good agreement between the calculated σ_f/σ_c
and the experimental σ_f/σ_R of Sikkeland and Viola, as the
excitation energy increases, the σ_f/σ_c curve is found to
deviate from the σ_f/σ_R curve. Since nothing is known as to
the cause of this deviation, nothing can be said about the
manner in which it is expected to occur.

The following procedure was now adapted. The calcu-
lations were fitted to the lowest point of the Sikkeland-
Viola data (65 MeV of excitation for $Er^{170} + O^{16}$) by varying
a_n. This fit was done for two values of $(Z^2/A)_{crit}$. The
values of $(Z^2/A)_{crit}$ used were 50.12 and 48.4, which are

thought to be representative of the limits of uncertainty in this quantity (see footnote 32). Thus two fits were obtained. The other parameters were fixed as follows: ΔL_n = 2 units of $\hbar$; $\Delta_R = \Delta$; a_f = A/8. The choice of 2 units of $\hbar$ for the angular momentum carried off by neutrons is based on the work of Alexander and Simonoff.[50] As was shown earlier, another choice for ΔL_n would not change the conclusions reached here in any way. These fits gave what are thought to be upper and lower limits on the average quantities considered. Figs. IV-9 and IV-10 illustrate the fits to the lowest data point for $Er^{170} + O^{16}$ and $W^{182} + O^{16}$ respectively. The adjustable parameters used for $Yb^{174} + C^{12}$ were the same as those for $Er^{170} + O^{16}$ (since the same compound nucleus, Os^{186}, was formed), and the fit to the data was fairly good. Table IV-4 gives the parameters for the various curves. Table IV-5 gives the results of the calculations for the average quantities. The range in any given quantity indicated in Table IV-5 is the range defined by the maximum and minimum values of the two fits described above. Since the L values are a function of the radius parameter, r_o, their range in Table IV-5 is based on a range in r_o from 1.2 to 1.5 fermis. The following two features are apparent.

(a) The ranges calculated are relatively narrow for $\langle E_x \rangle$, $\langle E_x^{saddle} \rangle$, and $\langle \nu_p \rangle$. They are greater for $\langle L \rangle$.
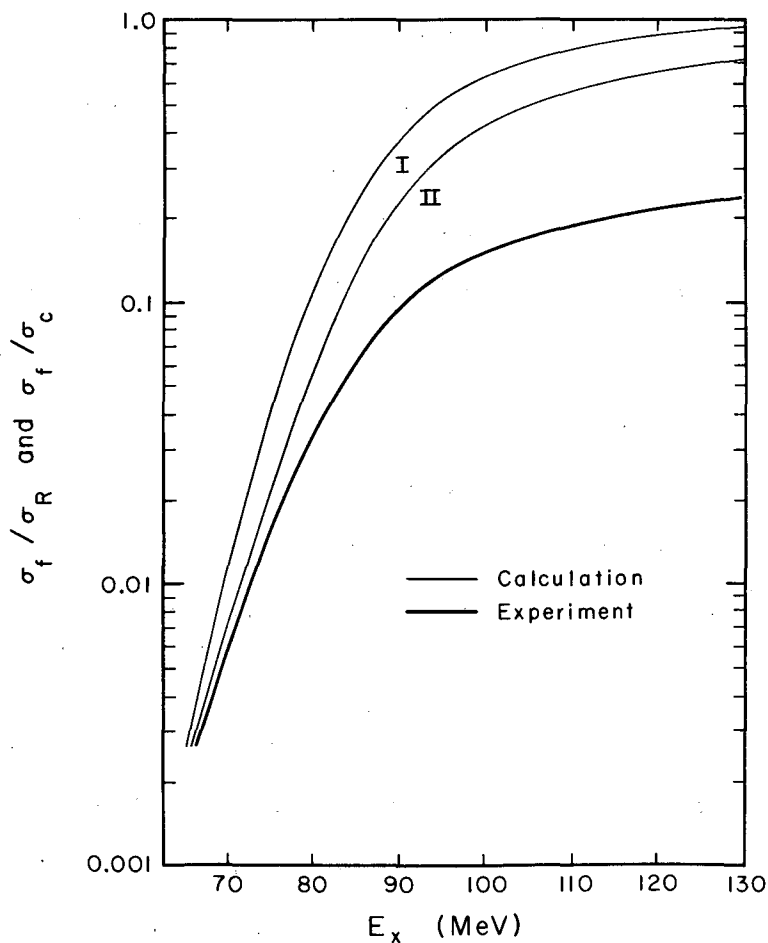
MU-33166

Figure IV-9.   Comparison of calculated σ_f/σ_c values with
experimental σ_f/σ_c values. Two different values
for $(Z^2/A)_{crit}$ have been used. The curves were
obtained by adjusting a_n until the calculated
ratio σ_f/σ_c coincides with the experimental
ratio σ_f/σ_R at 65 MeV excitation energy. These
curves are for the $Er^{170} + O^{16}$ reaction.
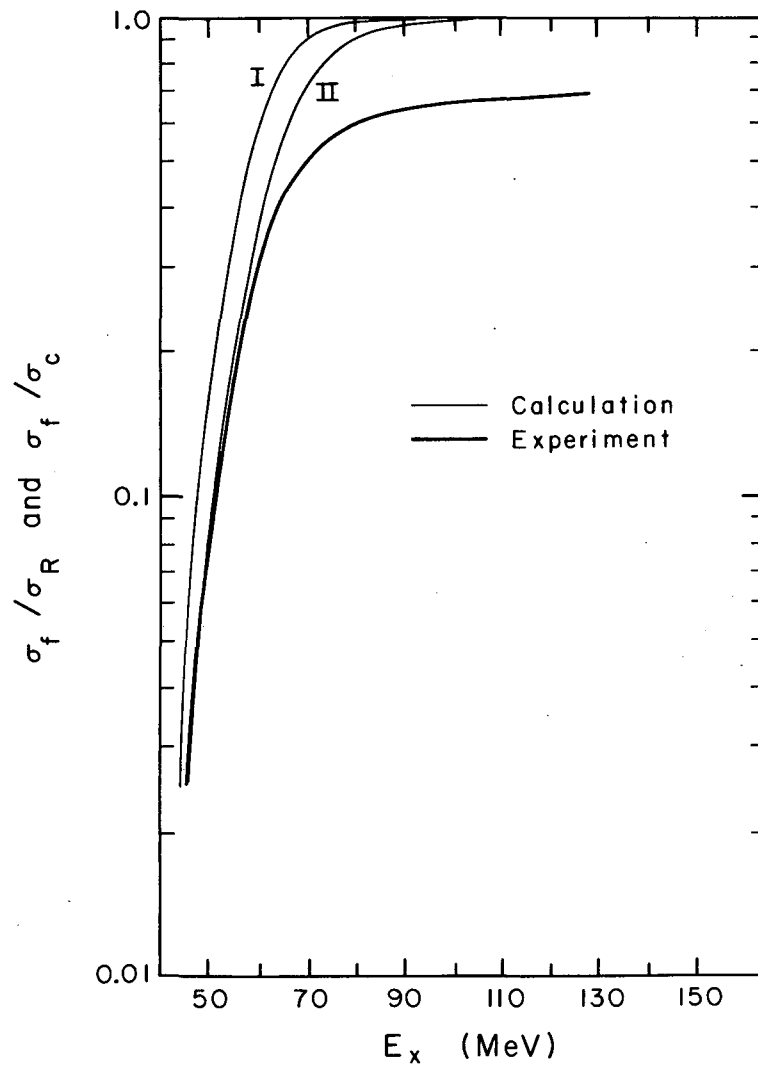
MU-33167

Figure IV-10. Comparison of experimental and calculated
excitation functions for the $W^{182}+O^{16}$
reaction. The calculations have been fitted
to experimental results at 45 MeV excitation
energy.

Table IV-4. Values of adjustable quantities used in curves of Figs. IV-9 and IV-10.

Figure	System	Curve Number	a_n	$(Z^2/A)_{crit}$
IV-9	$Er^{170}+O^{16}$	I	A/9.9	50.12
		II	A/8.7	48.4
IV-10	$W^{182}+O^{16}$	I	A/10.6	50.12
		II	A/9.1	48.4

Other adjustable quantities used in this table are $a_f = A/8$, $\Delta L_n = 2$ units of $\hbar$, and $\Delta_R = \Delta$ (the shell correction for the nonrotating nucleus).

Table IV-5. Ranges of average values of excitation energy, angular momentum, and number of pre-fission neutrons obtained from σ_f/σ_c calculations.

System	Bombarding Energy (MeV)	Initial Excitation Energy (MeV)	$\langle E_x \rangle$ (MeV)	$\langle E_x^{saddle} \rangle$ (MeV)	$\langle \nu_p \rangle$	$\langle L \rangle$	L_{max}
$Er^{170}+O^{16}$	165	129	120-128	96±3	0.1-0.7	50-72	75-94
	151	116	106-115	83±3	0.1-0.8	48-69	70-87
	136	103	90-101	68±3	0.2-1.0	47-65	63-79
	120	88	72- 85	50±3	0.3-1.3	44-59	54-68
$Yb^{174}+C^{12}$	125	103	84- 99	67±6	0.3-1.5	42-59	56-70
	109	88	72- 85	53±4	0.2-1.3	40-53	49-62
$W^{182}+O^{16}$	165	126	125-126	104±2	0 -0.1	50-63	–
	144	106	104-106	85±1	0 -0.2	43-55	–
	127	92	86- 91	70+1	0 -0.4	38-48	–
	115	80	73- 80	58±1	0 -0.6	33-43	–
	102	68	59- 67	45±2	0.1-0.8	28-37	–

(b) The absolute magnitude of $\langle \nu_p \rangle$ is relatively small. This is an encouraging result, since it tends to make the excitation energies well defined. $\langle \nu_p \rangle$ seldom exceeds 1. This result changes only when the difference between σ_f/σ_c and σ_f/σ_R in the fits discussed above is of the order of a magnitude in the region of low excitation energies. This may occur, for example, when the relative values of a_f and a_n are different from those used in the final calculations presented here (Table IV-4).

V. RESULTS AND DISCUSSION

A. General Comparisons and Effects of Excitation Energy

Section II of this work described how correlated two-dimensional measurements were made of the energies of both fission fragments from every event considered. Section III described how the calibration and corrections were applied and how the coordinates of the density-of-events distribution were transformed from the two energies E_1 and E_2 of the fragments to the mass, A_1, of one fragment and the total kinetic energy, E_T, released in the process. Other parts of Section III dealt with the calculation of statistical moments of the probability distributions, and with the calculation of corrections for the effect of neutrons on these statistical moments. Thus the data are now ready for a direct comparison with the theoretical mass-total kinetic energy distributions discussed in Section IV.

In making comparisons between experiment and theory, it should be remembered that:

(a) The theory does not include the use of any adjustable parameters, and the experimental distributions have not been normalized to the theoretical ones in any way.

(b) The theory calculates distributions before the emission of neutrons, while the experimental distributions are measured after neutron emission.

(c) The theory of Nix and Swiatecki in its present state
of development does not include angular momentum effects.
Angular momentum has been taken into account only in a pre-
liminary way when fission barriers were considered.

Due to the nature of the corrections for the effect
of neutron emission from fragments (Part I of Section III),
when experimental overall distributions are presented, they
do not include neutron corrections. When the moments of the
experimental distributions are presented, however, they are
corrected for neutron effects. In the figures presented
here the cases in which no neutron correction has been made
are pointed out by an asterisk superscript on the total
kinetic energy symbol (i.e., E_T^*).

1. Comparisons of Gross Features of the Distributions

Perhaps the most graphic illustration of the mass-
total kinetic energy distributions is given by contour lines
on a mass-total kinetic energy diagram. These contour dia-
grams are shown in Fig. V-1, which represents the case of
W^{182} bombarded with 102 MeV O^{16} ions. The lines pass through
regions of a constant density-of-events in the experimental
case (top part of the figure) and through regions of constant
probability of observing an event in the theoretical case
(bottom part of the figure). The units on the contours may
be considered to be arbitrary (the significance of the numbers
on the contours is that the 1000 contour would pass through
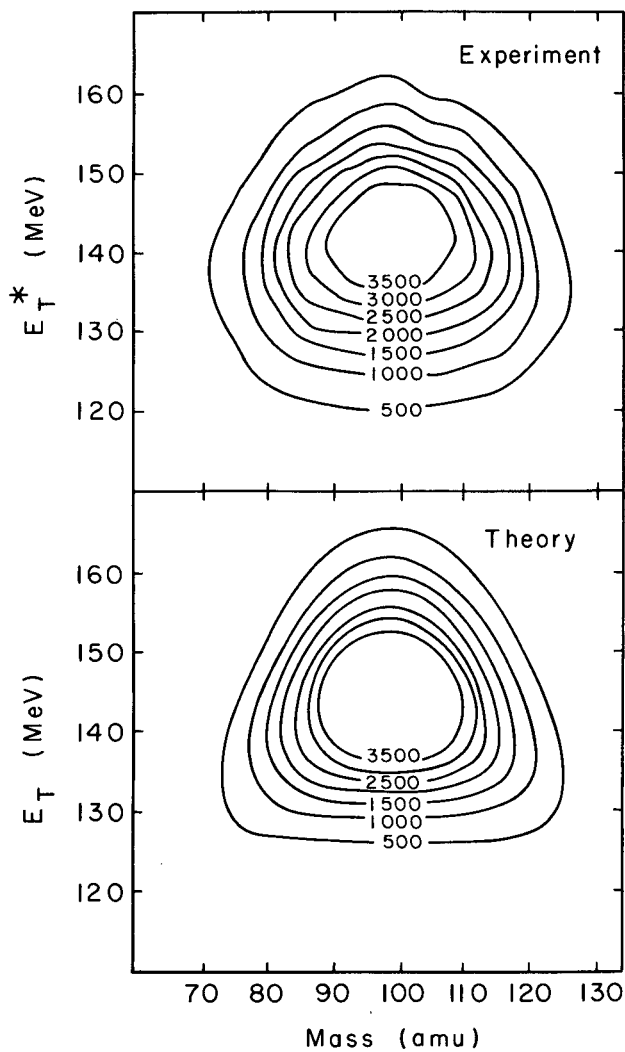
Figure V-1. Comparison of the experimental density of events distributions (top) with the theoretical probability distribution (bottom) in the E_T vs Mass plane for 102 MeV $O^{16}+W^{182}$. The experimental data are not corrected for neutron effects.

all regions of the plane where an area of 3 mass units by
6 MeV would contain 1% of the total number of events). The
theoretical and experimental contour diagrams are directly
comparable except for the effects of neutron emission from
the fragments. As was mentioned in Section III, this effect
consists primarily of a decrease in total kinetic energy,
making E_T larger than E_T^*. The neutrons, however, also affect
the width of the distributions (primarily at the wings, as
was illustrated in reference 4). With these reservations
in mind, the top and bottom halves in Fig. V-1 may be cautiously
compared. The general conclusion is that the two distributions
look quite similar, and have approximately the same width.
The edges of the triangular theoretical distribution have,
however, been rounded off to some extent in the experimental
distribution. This is a feature which will persist through-
out the further comparisons made in this work and will be
discussed in the subsection dealing with the fine features
of the distributions. Further comparisons are, in fact,
only further examinations (sometimes with the help of
statistical moments) of the contour diagrams of the type shown
in Fig. V-1.

We now turn to examine the widths of the overall
total kinetic energy-yield and mass-yield distributions
(these are obtained from the two-dimensional distributions
by summation in the appropriate direction). They are presented

in Figs. V-2 to V-9. Only the distributions for maximum
and minimum bombarding energies are shown here for each of
the compound nuclei studied (Os^{186} and Pb^{198}). To illustrate
the effect of broadening width with increasing excitation
energy, it was desirable in all cases to superimpose the peaks
of the two E_T-yield distributions shown on the same graph.
This resulted, in some cases, in a slight shift in the E_T
scales for one distribution relative to the other. Both
scales are given in the figures. The above remarks concern-
ing neutron emission again apply. In this case, the neglect
of neutron effects manifests itself in the value of E_T^* at
the peak of the theoretical distribution. No such neutron
effects in the mass-yield curve need be considered for
reasons discussed earlier (see Section III and Appendix C).
Table V-1 is a key to Figs. V-2 to V-9. These curves show
that the width of the overall distributions increases with
increasing excitation energy, as is expected from theory.

This increase in width as the bombarding energy is
increased is illustrated more quantitatively in Figs. V-10
to V-13. These figures show the variances of the overall
distributions discussed above as a function of the nuclear
temperature. (The variance is a measure of the square of
the width of a distribution.) The data points in these
figures are corrected for neutron effects. The nuclear
temperature θ in these comparisons is the temperature at the

Table V-1. Key to figures of overall distributions.

System	Bombarding Energy (MeV)	Type of Distribution	Experiment		Theory	
			Fig. No.	Symbol	Fig. No.	Curve No.
$Er^{170}+O^{16}$	120	E_T-yield	V-2	Closed Circles	V-3	I
	165			Open Circles		II
$W^{182}+O^{16}$	102	E_T-yield	V-4	Closed Circles	V-5	I
	165			Open Circles		II
$Er^{170}+O^{16}$	120	Mass-yield	V-6	Closed Circles	V-7	I
	165			Open Circles		II
$W^{182}+O^{16}$	102	Mass-yield	V-8	Closed Circles	V-9	I
	165			Open Circles		II
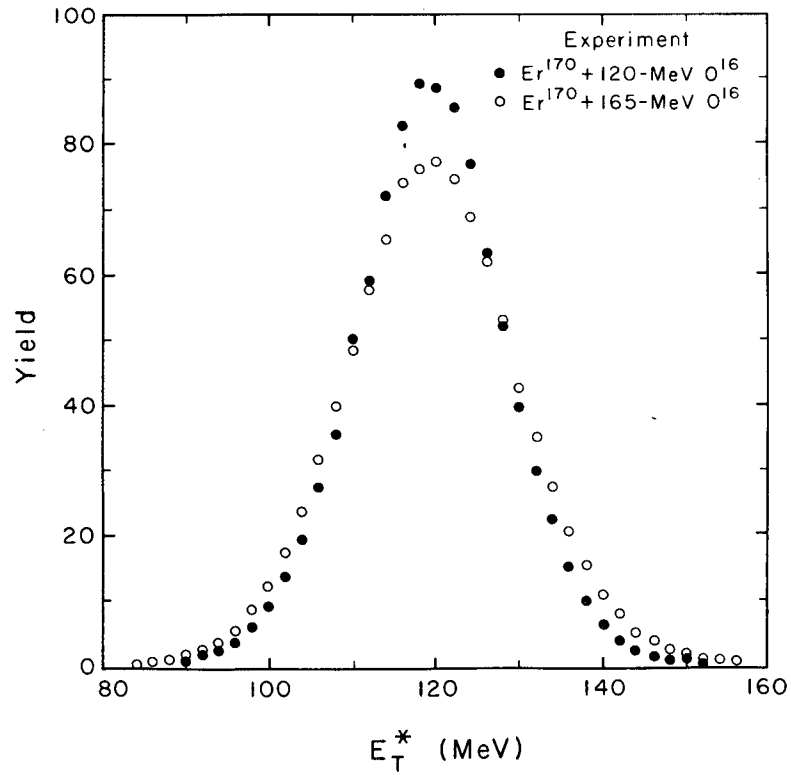
MU-33169

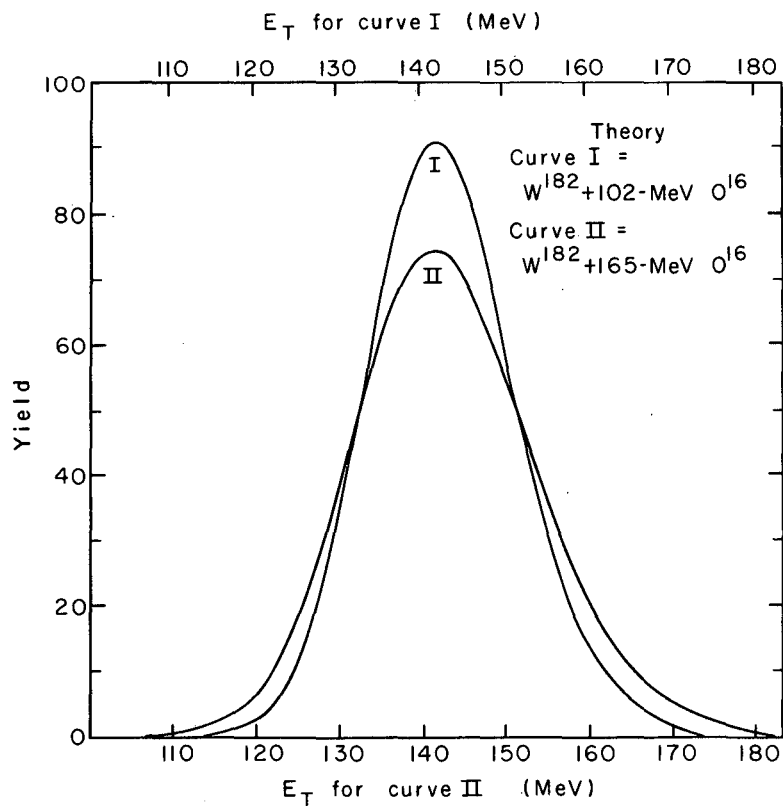Figure V-2. Uncorrected yield-total kinetic energy distributions for the $O^{16}+Er^{170}$ bombardment.
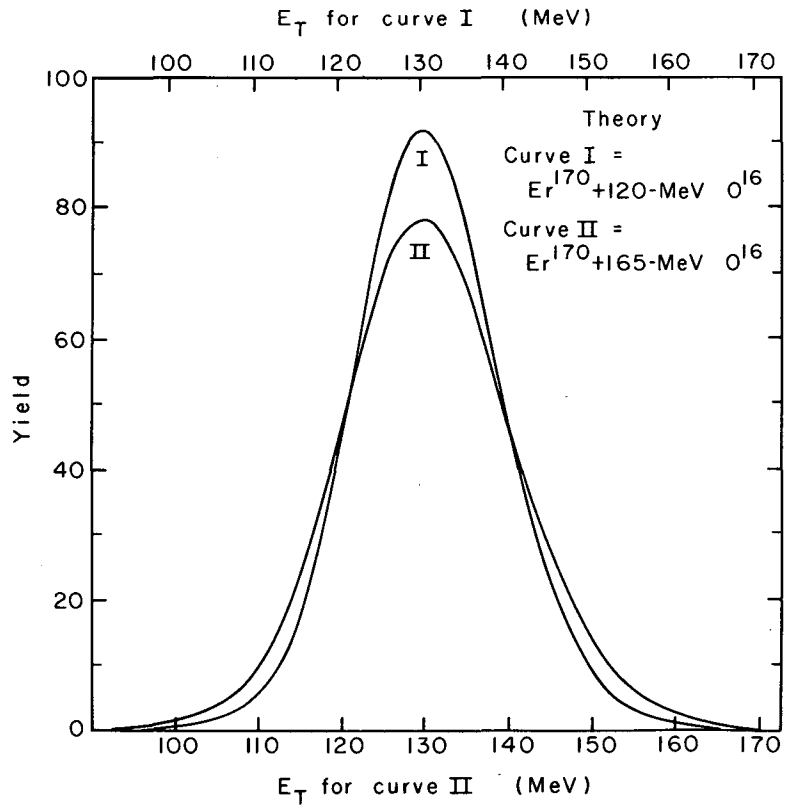
Figure V-3. Theoretical yield-total kinetic energy distri-
butions for the case of Fig. V-2. Curve I
corresponds to closed circles of Fig. V-2, and
curve II to open circles.

E* for closed circles (MeV)

110 120 130 140 150 160 170

100

Experiment

• W^{182}+102-MeV O^{16}

80

○ W^{182}+165-MeV O^{16}

Yield

60

40

20

0

110 120 130 140 150 160 170

E* for open circles (MeV)
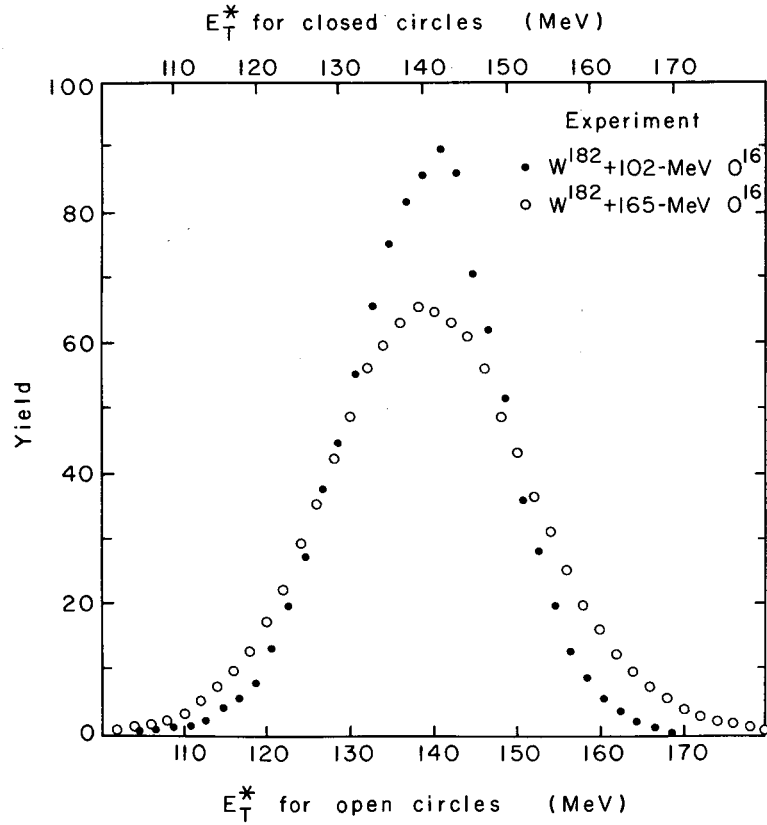
MU-33171

Figure V-4. Experimental yield-total kinetic energy distri-
butions for fission induced by bombardment of
W^{182} with O^{16} ions.

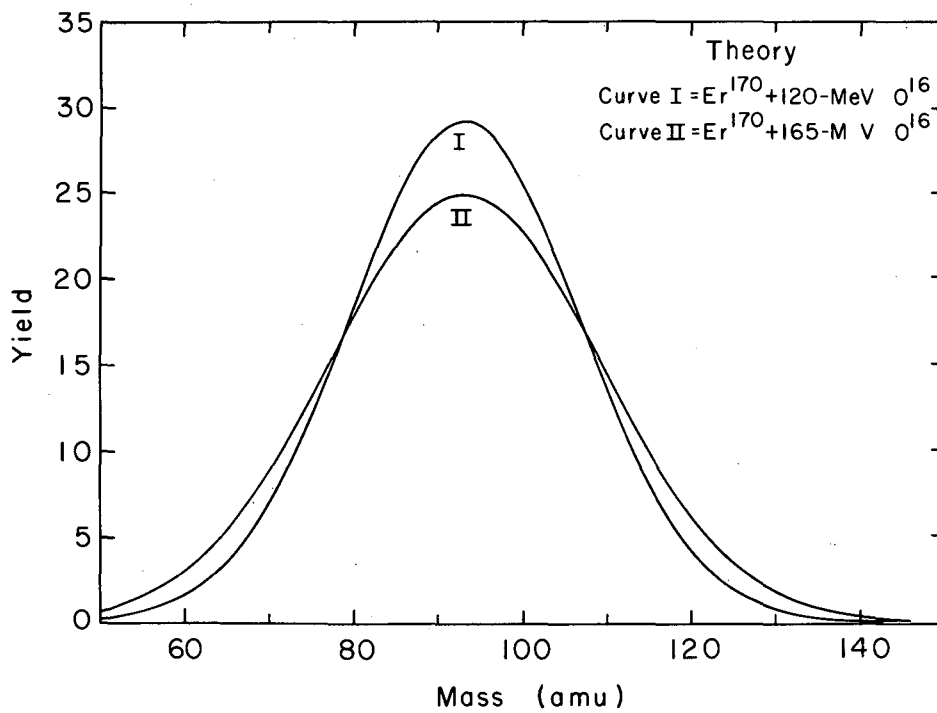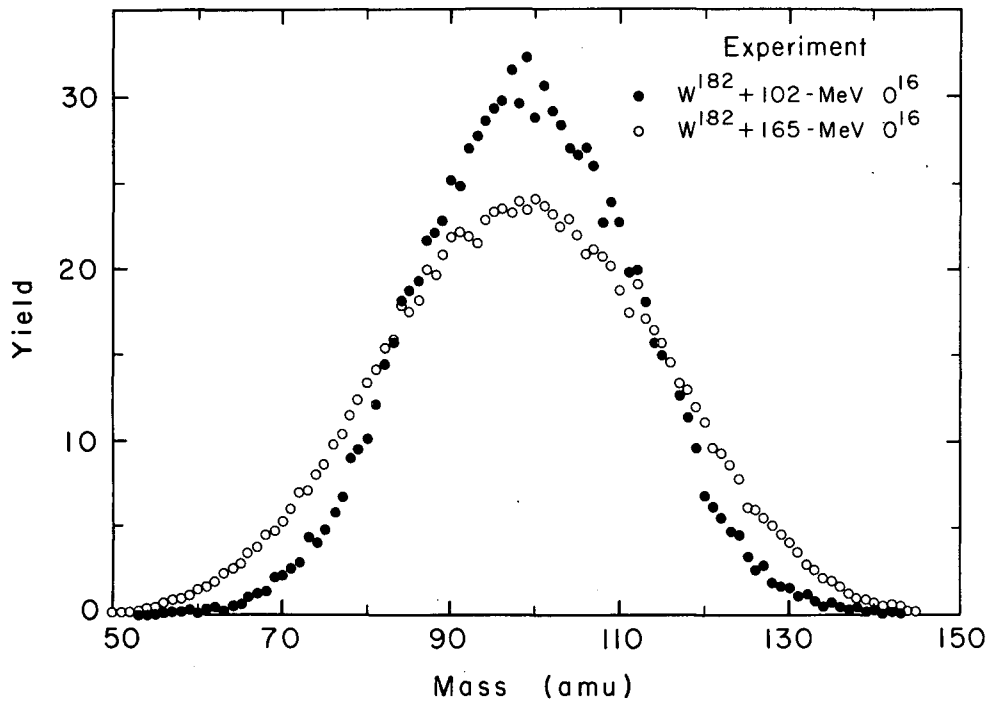Figure V-5.   Theoretical yield-total kinetic energy distributions for the same cases as Fig. V-4.
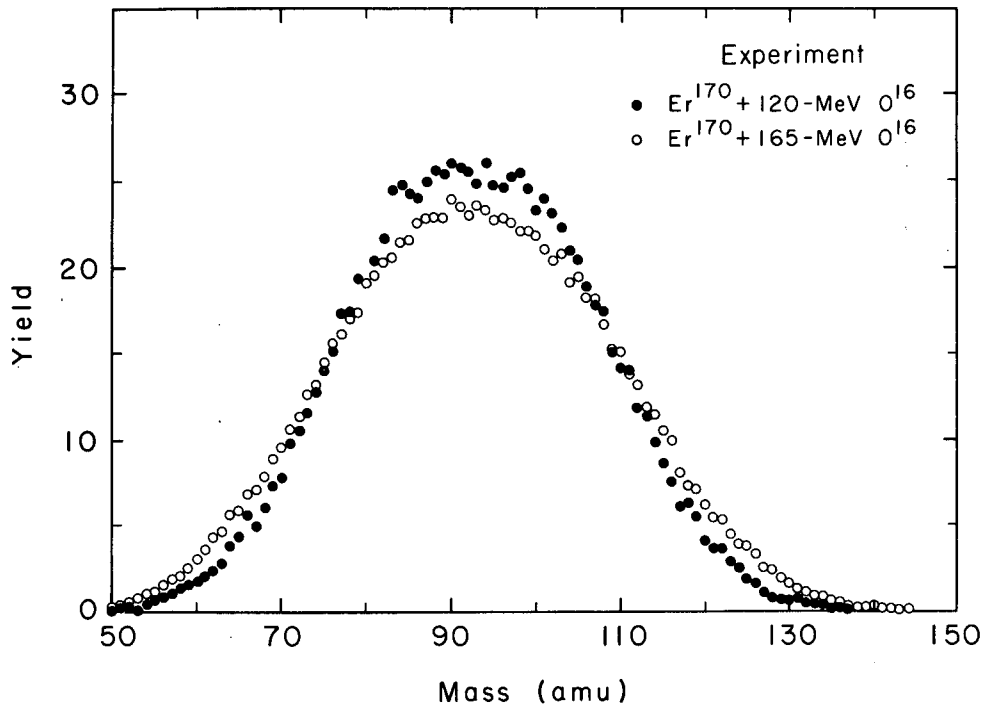
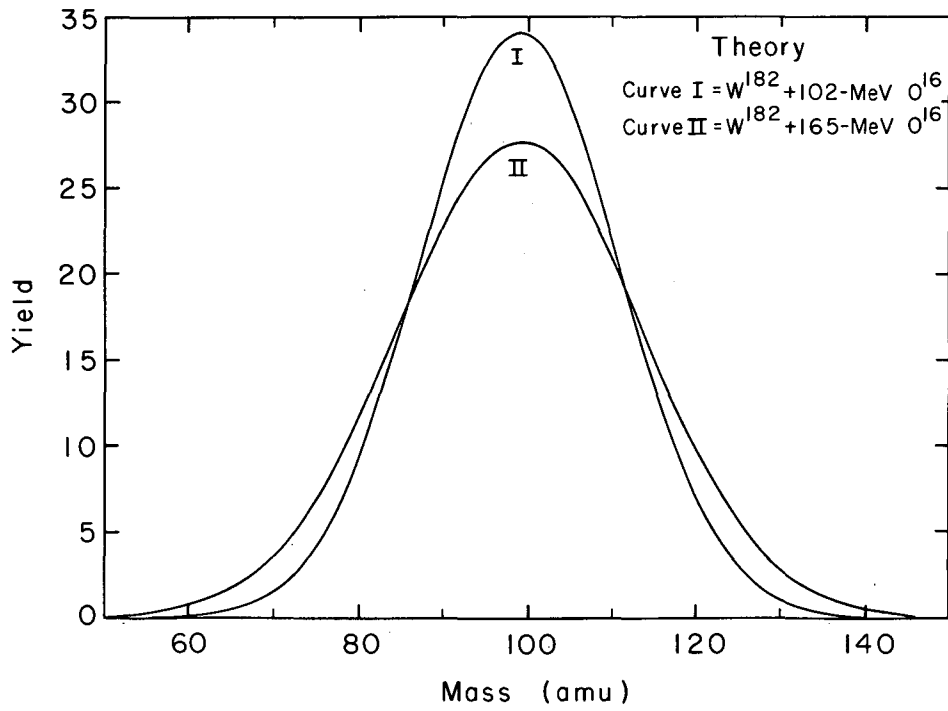Figure V-6. Experimental mass-yield distributions for the $O^{16}+Er^{170}$ case.

Figure V-7. Theoretical mass-yield curves for the case of Fig. V-6.

Figure V-8.   Experimental mass-yield distributions for the
$O^{16}+W^{182}$ case.

Figure V-9. Theoretical mass-yield curves for the same cases as those of Fig. V-8.

saddle. It is obtained from the excitation at the saddle, E_x^{saddle}, of Table IV-5, using the relationship[44]

$$E_x^{saddle} = a\theta^2 - \theta$$

where a is the level density parameter, taken to be equal to A/8. Table V-2 is a guide to Figs. V-10 to V-13. The solid lines represent the theoretical calculations. The vertical error bars on the experimental points have been estimated on the basis of errors introduced by choice of calibration scheme, and errors in neutron corrections. The horizontal error bars are based arbitrarily on double the estimated errors in $\langle E_x^{saddle} \rangle$ of Table IV-5. The $Bi^{209} + He^4$ point is that of Burnett[4] and represents a different compound nucleus from Pb^{198} studied here. It has, however, the same value of the fissionability parameter, x, as the Pb^{198} compound nucleus. The data used in these figures are tabulated in Table V-3, along with the average value $\langle E_T \rangle$ of the overall total kinetic energy distributions.

The agreement, on the whole, is remarkably good. The work of Burnett[4] showed for the first time that the liquid drop calculations and the corresponding measured quantities agree in magnitude (at a certain temperature). The present work shows that the variation of the overall width of the distributions with temperature is also accounted for by the liquid drop model. Thus the gross features of the mass-total kinetic energy distributions are reproducible in magnitude and

Table V-2. Key to figures of variance of overall distribution
as a function of temperature.

| Figure Number	System	Distribution	Symbol
V-10	$Er^{170}+O^{16}=Os^{186}$	E_T-yield	Closed Circles
	$Yb^{174}+C^{12}=Os^{186}$	E_T-yield	Open Circles
V-11	$W^{182}+O^{16}=Pb^{198}$	E_T-yield	Closed Circles
	$Bi^{209}+He^{4}=At^{213}$	E_T-yield	Open Circles
V-12	$Er^{170}+O^{16}=Os^{186}$	Mass-yield	Closed Circles
	$Yb^{174}+C^{12}=Os^{186}$	Mass-yield	Open Circles
V-13	$W^{182}+O^{16}=Pb^{198}$	Mass-yield	Closed Circles
	$Bi^{209}+He^{4}=At^{213}$	Mass-yield	Open Circles
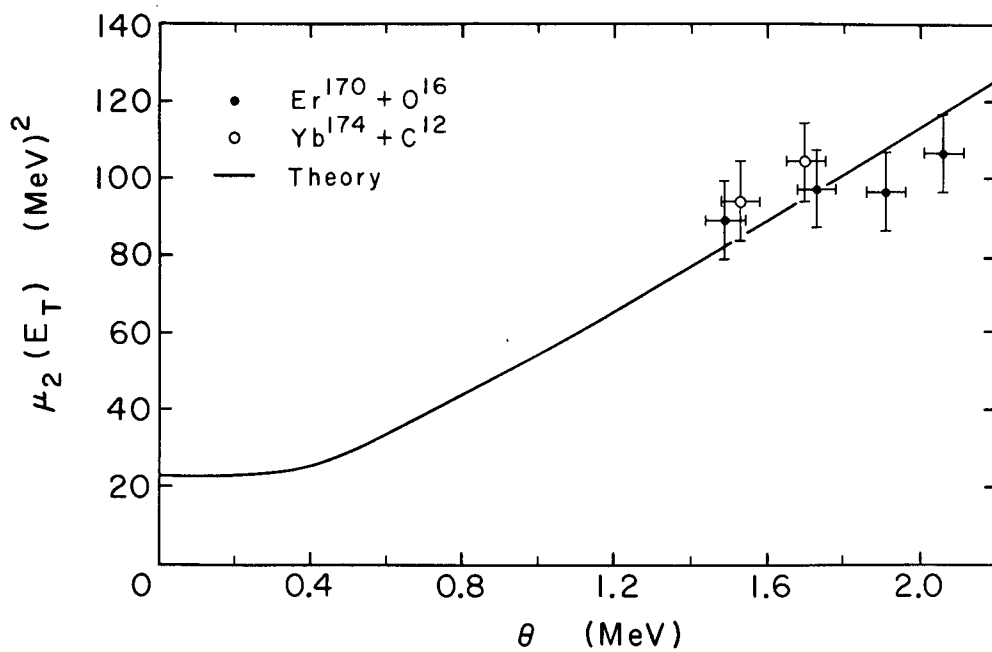
MU-33177

Figure V-10. Variances of the overall total kinetic energy distributions as a function of temperature for the case of the Os^{186} compound nucleus.
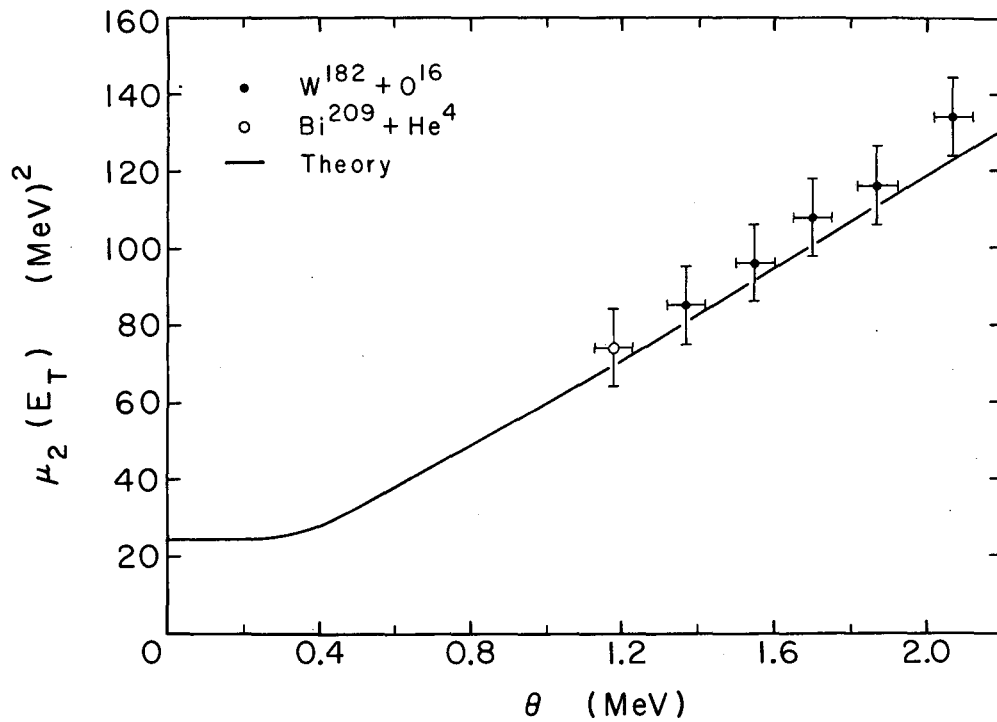
MU-33178

Figure V-11. Variances of the overall total kinetic energy for the Pb^{198} compound nucleus. The open circle denotes the reaction $Bi^{209} + He^4 = At^{213}$. At^{213} and Pb^{198} have the same value of the fissionability parameter x.
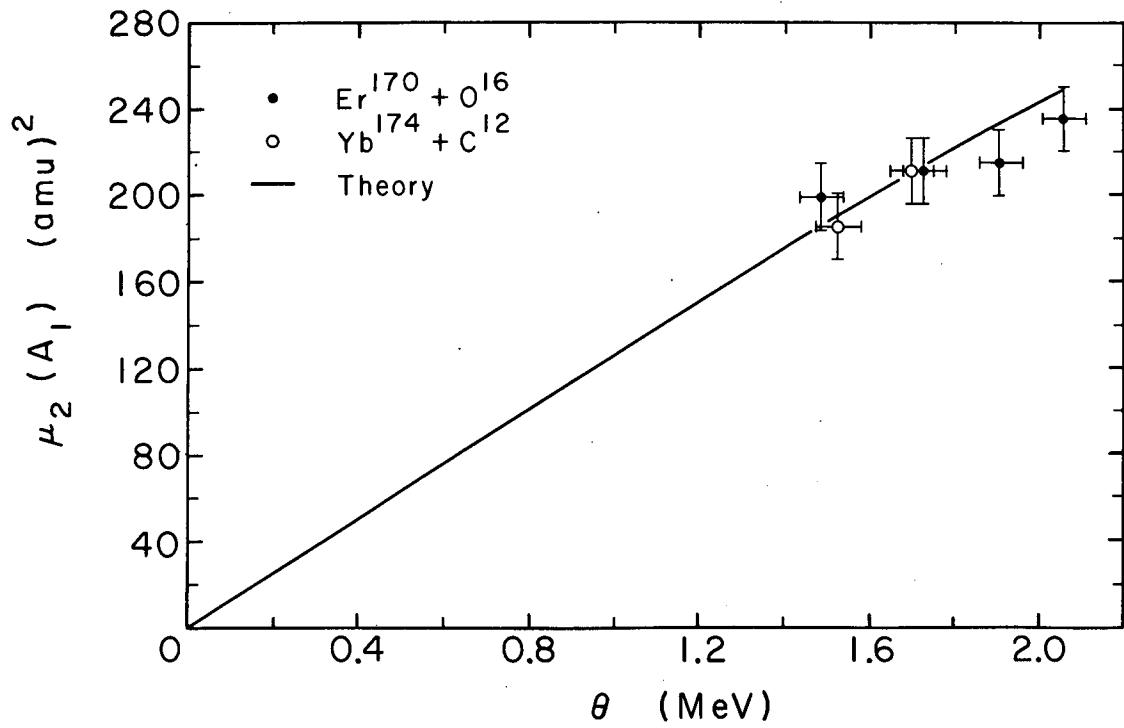
MU-33179

Figure V-12. The variances of the overall mass distributions as a function of temperature for the Os^{186} case.
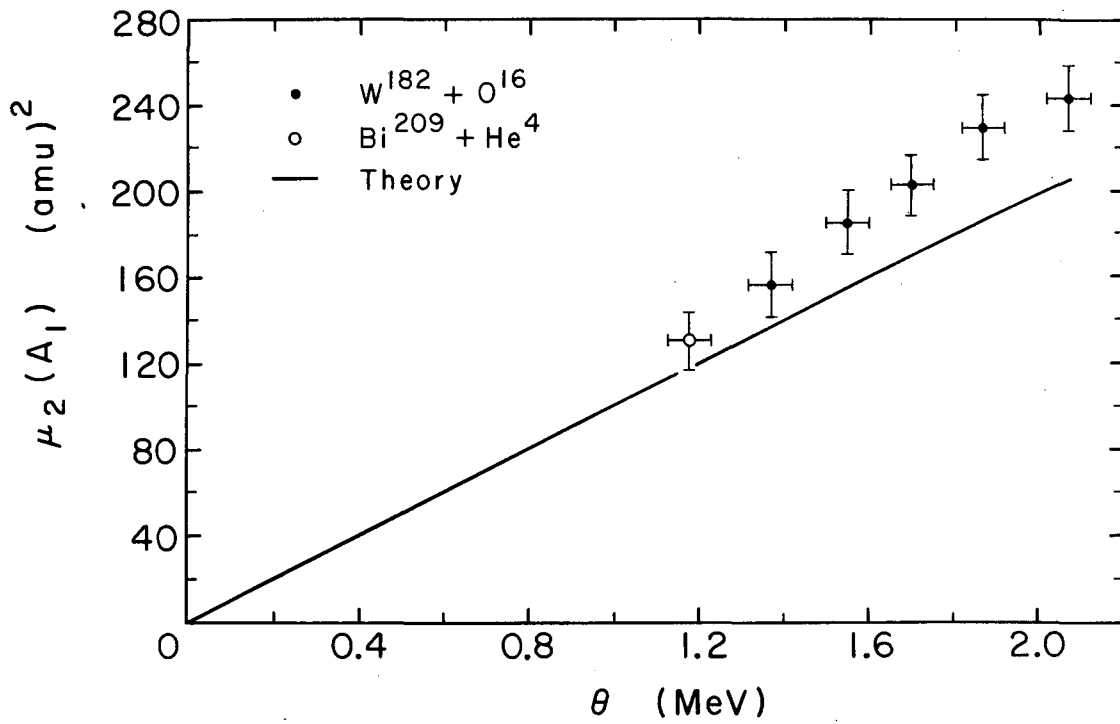
Figure V-13. Variances of the overall mass-yield curves for
the Pb^{198} case.

Table V-3. Comparison of theoretical and experimental overall moments of mass and total kinetic energy distributions.

System	Bombarding Energy (MeV)	θ (MeV)	$\langle E_T \rangle$		$\mu_2(E_T)$		$\mu_2(A_1)$	
			Exp. (MeV)	Theory	Exp. (MeV)^2	Theory	Exp. (amu)^2	Theory
$Er^{170}+O^{16}$	165	$2.06\pm.05$	127 ± 6	131	106 ± 10	116	235 ± 15	249
	151	$1.91\pm.05$	128 ± 6	131	96 ± 10	108	215 ± 15	234
	136	$1.73\pm.05$	124 ± 6	131	97 ± 10	97	211 ± 15	213
	120	$1.49\pm.05$	124 ± 6	131	89 ± 10	82	199 ± 15	186
$Yb^{174}+C^{12}$	125	$1.70\pm.05$	129 ± 6	131	104 ± 10	95	211 ± 15	211
	109	$1.53\pm.05$	127 ± 6	131	94 ± 10	85	185 ± 15	190
$W^{182}+O^{16}$	165	$2.07\pm.05$	147 ± 5	143	134 ± 10	123	243 ± 15	205
	144	$1.87\pm.05$	146 ± 5	143	116 ± 10	111	229 ± 15	186
	127	$1.70\pm.05$	146 ± 5	143	108 ± 10	101	203 ± 15	170
	115	$1.55\pm.05$	144 ± 5	143	96 ± 10	92	185 ± 15	155
	102	$1.37\pm.05$	144 ± 5	143	85 ± 10	81	156 ± 15	137

in their variation with temperature by an approximate version
of the liquid drop model.

The scatter in the measured points in the Os^{186} case
is believed to be due to experimental causes. As was discussed
in Section II, the data were collected over longer periods of
time than the Pb^{198} data, and a considerable amount of
addition of data from several experiments had to be made.
In the Pb^{198} case, where the experimental results are self-
consistent, excellent agreement was obtained over a large
range in θ for the variance of the E_T-yield distribution.
There was some disagreement between theory and experiment in
the widths of the mass-yield distributions in the Pb^{198} case
at high excitation energies. This disagreement, however, is
not very large, and will be reconsidered later.

2. Comparisons of Fine Features of the Distributions

We will find that in comparing the fine features of
the theoretical distributions with the experimental distri-
butions more disagreement will be apparent than was found
when the gross features of the distributions were considered.

We can examine the two-dimensional distributions in
greater detail by considering sections of the distribution
at various points and examining the width and average value
of the resulting profile distributions. Thus we will consider
the average value, $\langle E_T \rangle$, and variance, $\varkappa_2(E_T)$, of the E_T
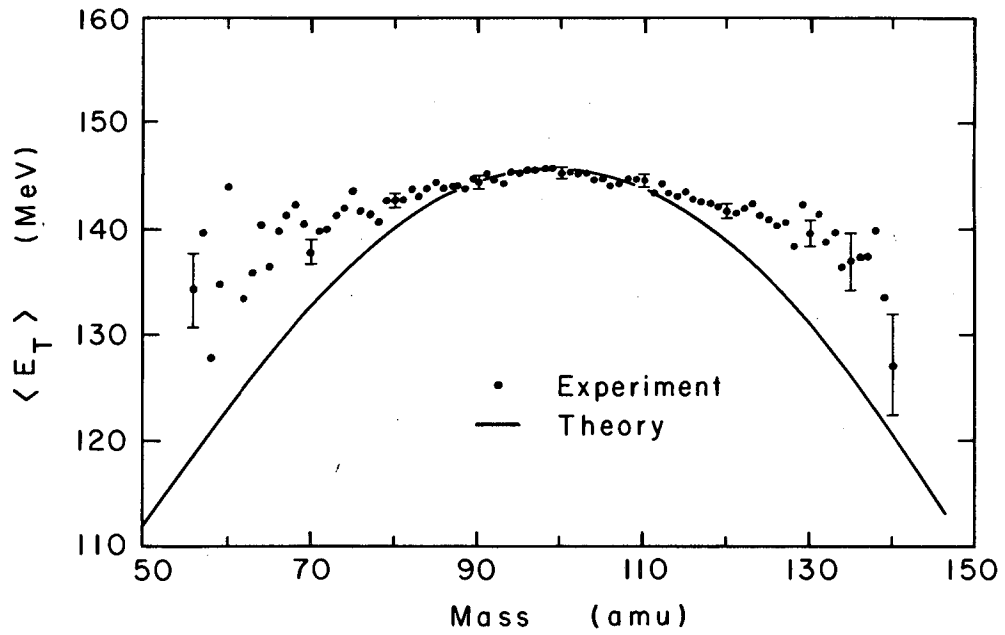distributions as a function of mass and the variance of the

mass distributions, $\mu_2(A_1)$, as a function of E_T. The following problems were encountered:

(a) The number of counts available was too small at the edges of the distributions to enable us to draw any conclusions from some of the calculated moments.

(b) The patterns that emerged from this study of variances were limited, and it was not thought profitable to present $\mu_2(E_T)$ versus A_1 and $\mu_2(A_1)$ versus E_T curves for all reactions studied. Two representative reactions only are illustrated, and conclusions drawn are limited.

(c) As will be seen, the disagreements between theory and experiment occur to the largest extent at the edges of the distribution. In addition to the problem of large statistical errors, any errors resulting from neutron correction procedures are also likely to be increased in these regions.

Figures V-14 and V-15 give comparisons between experimental and theoretical average total kinetic energy versus mass curves for the case of O^{16} and W^{182}. The deviation of the experimental curve from the theoretical one, which was just distinguishable in equivalent curves of reference 4, has become more pronounced in the 102 MeV (bombarding energy) case (Fig. V-14) and is very striking in the 165 MeV case (Fig. V-15). The errors shown in the figures represent statistical errors only. Since the reactions studied here differ from those studied by Burnett[4] mainly in

MU-33181

Figure V-14. Average values of the distributions in total kinetic energy as a function of mass for fission following the bombardment of W^{182} with 102 MeV O^{16} ions.
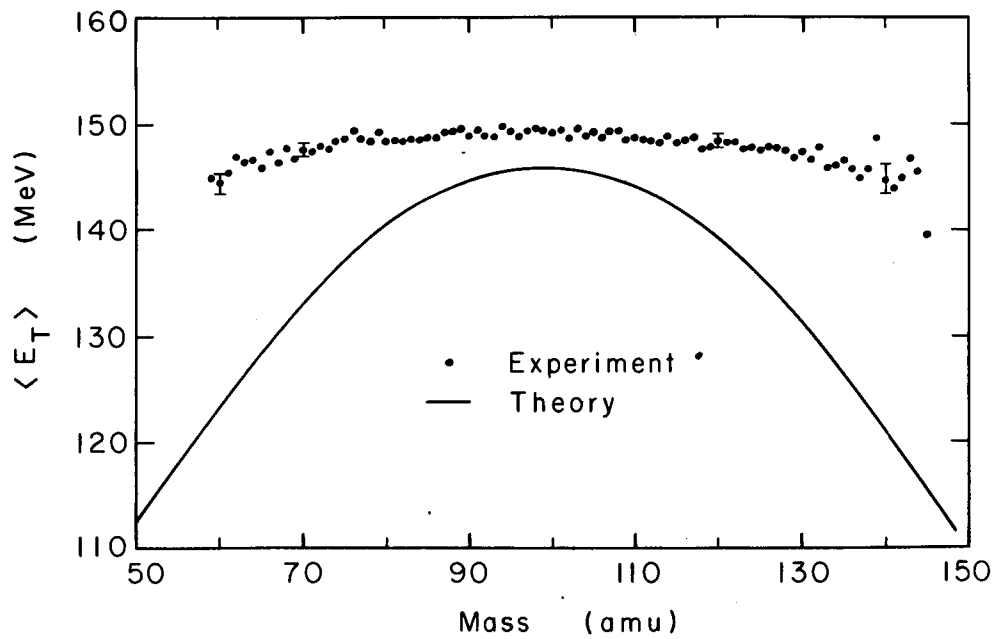
MU-33182

Figure V-15. Average values of the distributions in total
kinetic energy as a function of mass for fission
following the bombardment of W^{182} with 165 MeV
O^{16} ions.

the amount of angular momenta in the systems, it is possible
that this deviation is to a large extent due to this effect.
This is consistent with the fact that the deviation is greater
for greater bombarding energies.

Figures V-16 and V-17 show the variance of the total
kinetic energy distribution as a function of mass for O^{16}
and W^{182}. The bombarding energies are 102 MeV in Fig. V-16
and 165 MeV in Fig. V-17. The theoretical curve is given, as
in all these comparisons, by the solid line. It can be seen
that near the center of the distributions the agreement may
be quite good, and that the scatter of experimental points
near the edges is so large that not even the overall curva-
ture can be determined. Thus, while these results do not
contradict the speculation of Burnett[4] that agreement for
these quantities may be better for fission of elements
lighter than those he has studied, it does not conclusively
support it.

Figures V-18 and V-19 show the variance of the mass
distribution as a function of E_T for the same cases as Figs.
V-16 and V-17 respectively. As in reference 4, the slopes
of the experimental and theoretical curves do not agree.
This disagreement is again progressively worse as the bom-
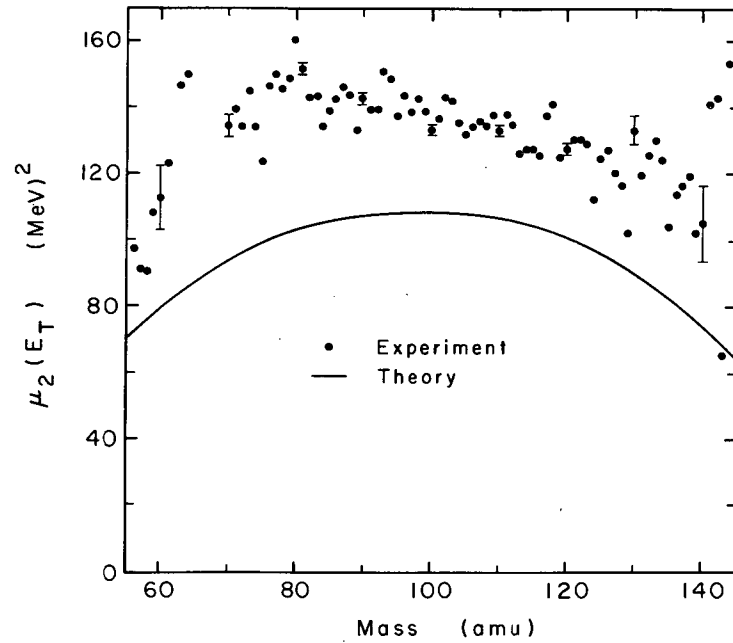barding energy increases.

B. Effects of Angular Momentum

As was mentioned earlier in this section, certain
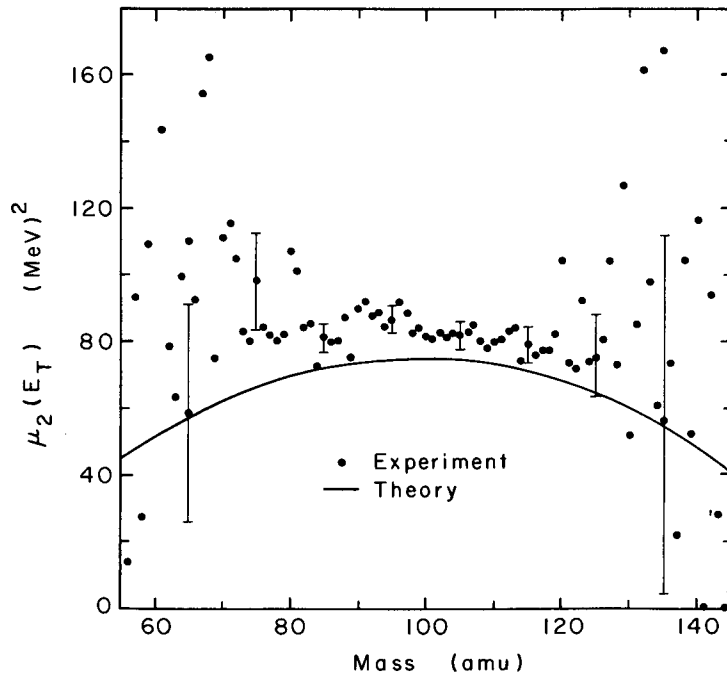
MU-33183

Figure V-16. The variances of the total kinetic energy distributions as a function of mass for the 102 MeV O^{16} on W^{182} case.
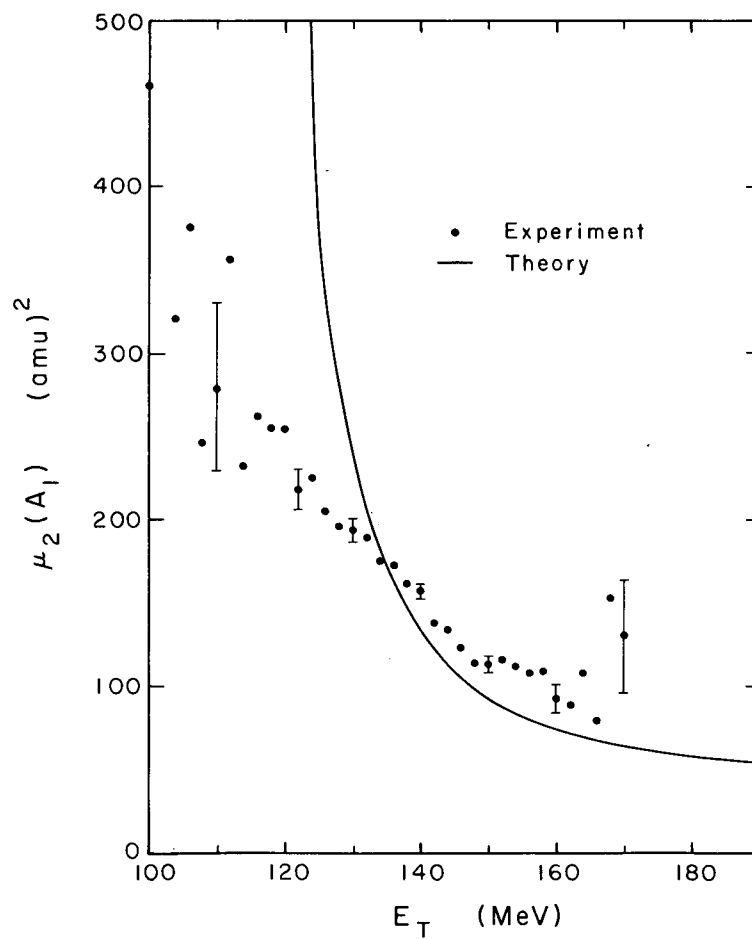
MU-33184

Figure V-17.   The variances of the total kinetic energy distri-
butions as a function of mass for the 165 MeV
O^{16} on W^{182} case.

MU-33185

Figure V-18. Variances of the mass distributions as a function
of the total kinetic energy for fission induced
by 102 MeV O^{16} ions on W^{182}.
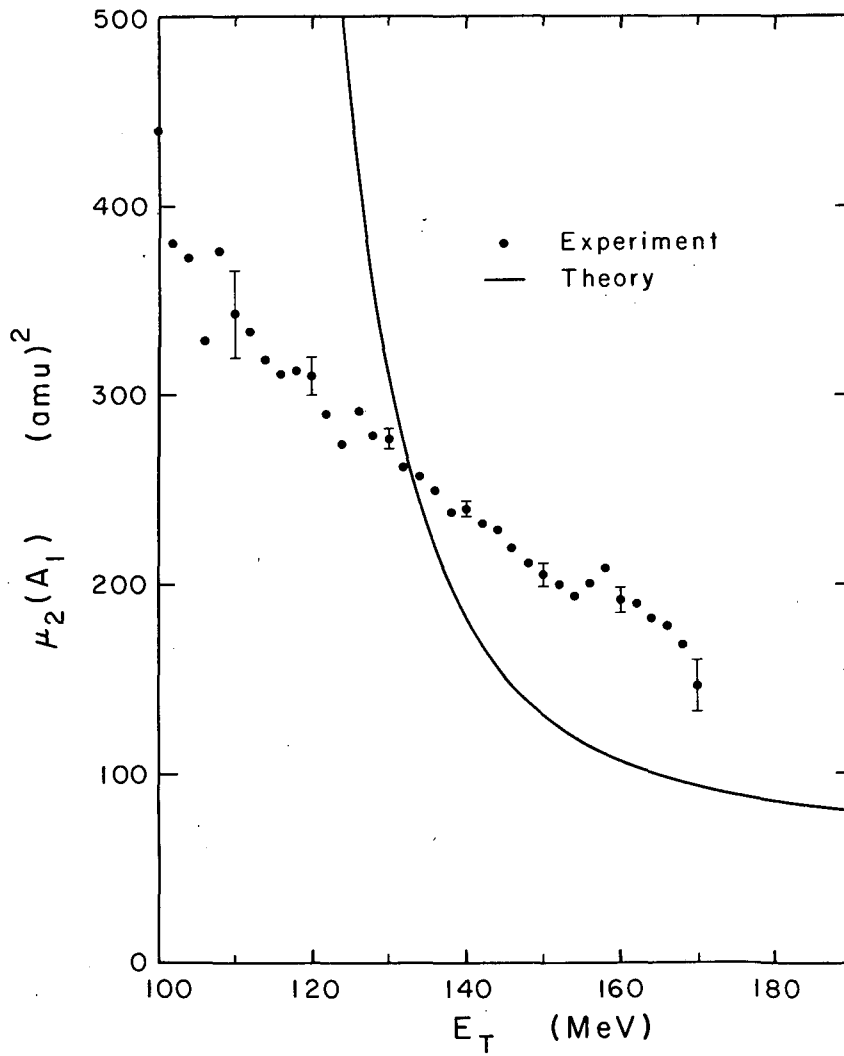
MU-33186

Figure V-19. Variances of the mass distributions as a function of the total kinetic energy for the W^{182} and 165 MeV O^{16} case.

disagreements found to be small in magnitude in α-induced fission[4,6] increased considerably in the heavy-ion-induced reactions considered here. Furthermore, these disagreements increased as the bombarding energy (and hence the angular momentum) increased. The possibility that these disagreements are in large part due to angular momentum effects certainly cannot be ruled out.

Considering the two reactions

$$Er^{170}+O^{16}=Os^{186}$$
$$Yb^{174}+C^{12}=Os^{186}$$
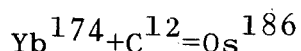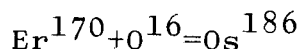
due to the difference in size of the projectiles, bombarding energies can be so adjusted as to produce compound nuclei with equal amounts of excitation energy, but different amounts of angular momentum (see Table IV-5). This difference in angular momentum was, however, not very large, which may account for the fact that no differences between the distributions resulting from these two reactions were observed. The largest effect of angular momentum is on the fission threshold and hence on the fission probability. This effect has been discussed fully in the theoretical section and is mentioned here for the sake of completeness.

C. Variations with Fissionability Parameter x

The theory predicts that as the fissionability parameter x increases, at a constant nuclear temperature, the width of the overall total kinetic energy distribution increases,

while the width of the mass-yield curve decreases. The first

of these predictions is found to be true experimentally, as

can be seen from Table V-3. The second, however, is not

found to be true. The width of the experimental mass distri-

bution is greater in the case of the Pb^{198} compound nucleus

than in the case of the Os^{186} compound nucleus. This causes

the deviation of experimental points from the theoretical

line to be greater in Fig. V-13 than in Fig. V-12.

Another prediction of the theory in its present state

of development that deserves mention is the following. If

the excitation energy is sufficiently high, and the x value

sufficiently low, the theoretical mass distributions at low

values of the total kinetic energy become asymmetric. This

is demonstrated in the lower part of Fig. V-20, which shows

a theoretical contour diagram of the type described in the

beginning of this section. It can be seen that the base

corners of the triangular distribution are "pulled down" so

that a cut across the distribution at $E_T \approx$ 115 MeV would result

in an asymmetric mass distribution. This two-dimensional

diagram is that for the case of $Er^{170}+O^{16}$ at 165 MeV bom-

barding energy. The corresponding experimental distribution

is shown in the top part of the figure. Although the

appearance of the asymmetry is expected to occur in a region

of such small density in events that it is on the limit of

experimental detection for the number of events measured in
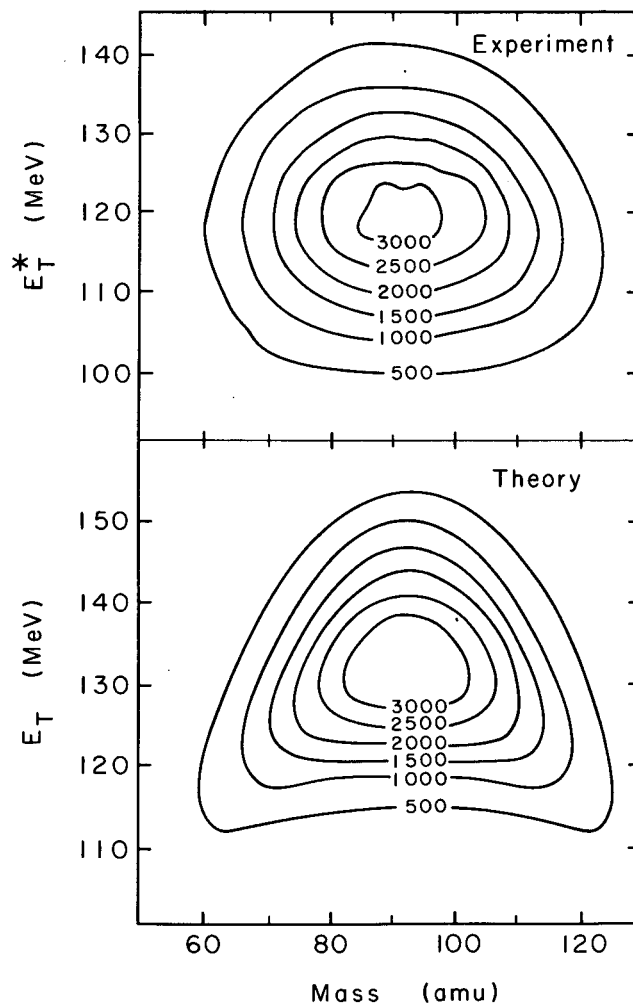
Figure V-20. Experimental and theoretical contour diagrams for the mass-total kinetic energy distribution for the 165 MeV O^{16} on Er^{170} case.

this work, the comparison in Fig. V-20 shows that no tendency at all exists in the experimental distribution toward this phenomenon. This seems to be yet another disagreement between experiment and theory at the edges of the distribution.

VI. CONCLUDING REMARKS

In the last section we have established that for the compound nuclei studied here, the liquid drop model (in its approximate spheroid version) is capable, without the use of any adjustable parameters, of accounting for the gross features of the mass-total kinetic energy distributions over a range of temperature. It was also found that differences between theory and experiment are present in some of the fine features of the distributions, particularly in the low density-of-events regions.

Since we have considered only two compound nuclei, and because of the uncertainties as to the reasons for any disagreement between experiment and theory, it does not, at the present time seem possible to give a complete evaluation of the overall ability of the liquid drop model to describe fission of elements in the low x region. This suggests an answer to the question of what experiments ought to be carried out in the future. These experiments should have two objectives in mind: they should (a) define the ranges in overall agreement and give a basis for the liquid drop theory at low x values; (b) define the nature and extent of the disagreements found in the fine features of the distributions.

The first purpose can best be followed up experimentally by making measurements of the type described here over a range of elements and at a number of excitation energies for each element

It has been hoped that the $Au^{197}+He^4$ data[6] could be used along with that from the two heavy ion reactions to compare data at three different values of x. Since the measurements on gold have, however, been made only at one energy, which was much lower than those studied here, this comparison was not found to be possible, and more data over a range of excitation energies are needed.

The second purpose mentioned above should be remembered in considering the following factors:

(a) Angular momentum effects in these measurements should be better evaluated. This can be done by studying the reaction:

$$W^{182}+He^4=Os^{186} .$$
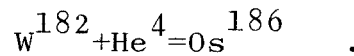
It is, however, only recently that He^4 beams of high enough energy have become obtainable to produce the Os^{186} compound nucleus at the same excitation as that produced from O^{16} bombardments of Er^{170}. Due to the small mass of the He^4 ions, the angular momenta involved would be much smaller.

(b) If the predicted effect of asymmetry at low values of the total kinetic energy is in fact more than a spurious by-product of the approximations made in the spheroid model, an attempt should be made to look for it under more ideal conditions. These would consist of an accumulation of a large number of fission events (about 5×10^5) using He^4 ions as projectiles (to eliminate angular momentum effects).

(c) An effort should be made to improve the overall

experimental accuracy of these measurements. Errors, such as result from a choice of calibration scheme, could be better understood if data from simultaneous energy (with solid state detectors) and velocity (with accurate time-of-flight techniques) measurements were available. Greater accuracy in measurement would give greater certainty to agreements and disagreements between theory and experiment, which could result in an estimate of the extent of shell effects on the fission process.

(d) Perhaps involving greater experimental difficulties, but certainly of great interest, would be measurements of neutron distributions. These measurements would not only make corrections to the data presented here more meaningful, but they could be compared in their own right with theory, since the neutrons are a measure of the de-excitation of the vibrating fragments, and the theory is capable of predicting the distribution of vibrational energy of the fragments.

(e) It must be remembered that the model of Nix and Swiatecki is only an approximation to the liquid drop model, which is already a simplified representation of true nuclei. Thus, for example, in the spheroid model used here the saddle point, being represented by two tangent spheroids, coincides exactly with the scission point. This is certainly not true in the real fission process. Recent calculations of Nix[40] seem to indicate that it will be possible to formulate a more

accurate model, which would also be adequate for the region of x from 0.67 to 0.8. This model will differ from the current one by the insertion of a hyperbolic neck between the two spheroids. Nix has been able to reproduce with remarkable accuracy the energies of deformation of Cohen and Swiatecki[2] by using this new model.

APPENDICES

A. Electronic System

A block diagram is shown in Fig. A. D1 and D2 represent the two fragment detectors. The linear system consists of two Goldsworthy Model VI amplifiers[16] and preamplifiers operated in their double-differentiating mode with rise times in the 0.2-1.0 μsec range. The variable feedback capacitor in the preamplifier was set at its maximum value of 13pF to make the output pulse-height as independent of detector capacitance as possible. To reduce the effect of changes in detector leakage current, the bias supply resistor was decreased from 22 to 0.5 megohms. The White follower outputs of the amplifiers were connected by means of short coaxial cables to the inputs of the two-dimensional analyzer. The cathode follower outputs of the amplifiers were used to drive variable delays and gates[17] (VDG), which in turn activated the fast-slow coincidence system (FSC). The cathode follower outputs also served as inputs to the two monitoring Penco pulse-height analyzers.

Pulses for the fast coincidence system (FC) were taken from the p-type side of the surface barrier detector[18] by connecting it to the 200Ω impedence input of a Hewlett-Packard distributed amplifier.[19] A total of six distributed amplifiers were used for each detector before the pulses were fed into a transistorised fast coincidence circuit capable of
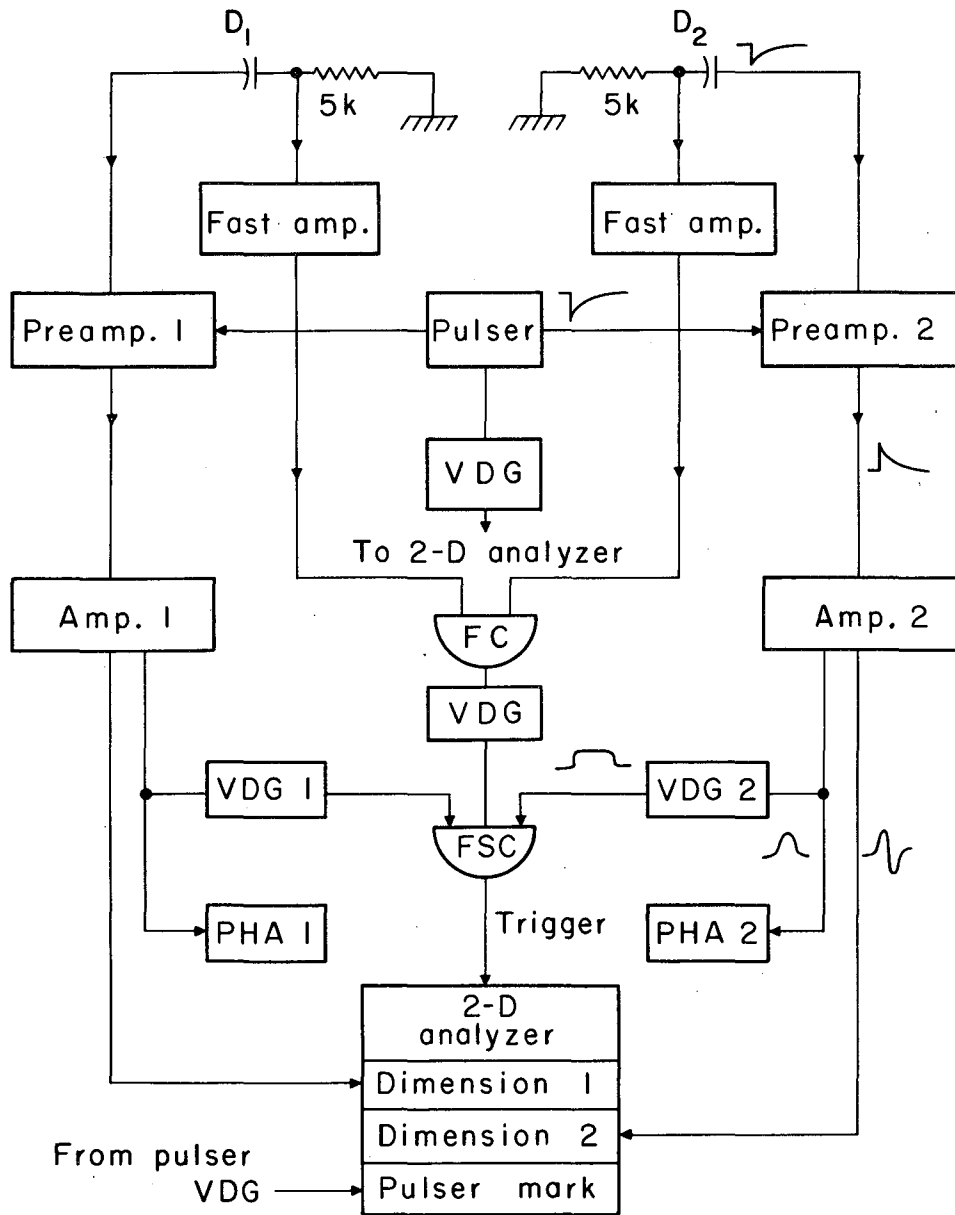
MUB-2342

Figure A. Schematic diagram of electronic equipment used in
the experiment. D1 and D2 are two surface barrier
solid state detectors. FC is the fast coincidence
system, and FSC is the fast-slow coincidence system.
VDG stands for variable delays and gates, and PHA
for pulse-height analyzers.

10^{-9} sec resolution time.[20] The 0.5 V negative output from this coincidence unit was fed via an inverting distributed amplifier to a 10-Mc discriminator-scaler.[21] All connections in the FC system were made with high impedance cable, with careful impedance matching at all points.

The fast-slow coincidence system (FSC) required coincidence between the two linear pulses and also the output from the 10-Mc discriminator. Its coincidence time of 10^{-6} sec would not have been by itself short enough to satisfy the timing requirements. It is included in this experiment to eliminate accidental coincidences due to possible bursts of noise feeding through the 10^{-8} sec FC system. VDG units were used to time phase the information for proper coincidence. The settings on the VDG units were set so as to allow all real fission events in which both fragments are detected to activate the slow coincidence unit.

The output from the slow coincidence unit served as a trigger to operate the first stage of the two-dimensional analyzer. This first stage consisted of two Penco analog-to-digital converters which gave out pulse trains depending in length on the size of the two input pulses. Scalers were used to count the number of pulses in each train, and the numbers were then stored in two consecutive positions of a small magnetic-core memory. After every twenty events, the memory was full, and its contents were transferred to an IBM

compatible magnetic tape.   The memory was cleared for further
data.

B. Estimate of the Average Number of Neutrons Evaporated from Fission Fragments

The average total number of neutrons, $\langle \nu_T \rangle$, evaporated from the two fission fragments was obtained from the following relationship, which is based on energy balance considerations:

$$\langle \nu_T \rangle = \frac{\langle E_R \rangle + \langle E_x \rangle - \langle E_T \rangle - \langle E_\gamma \rangle}{\langle B_n \rangle + \langle E_n \rangle} \quad .$$

$\langle E_R \rangle$ is the average energy released in fission, and $\langle B_n \rangle$ is the average binding energy for the neutrons emitted from the fragments. These two quantities were calculated using the program of Milton.[26] The results of this program were averaged over the experimental mass-yield curves. $\langle E_x \rangle$ is the average excitation energy of the fissioning nucleus, and its calculation is given in Section IV-D. $\langle E_T \rangle$ is the average total kinetic energy released in the fission considered. The measured total kinetic energy, $\langle E_T^* \rangle$, was corrected in the first approximation for neutron evaporation using the empirical formula of Leachman[27] for $\langle \nu_T \rangle$. $\langle E_n \rangle$ is the average neutron kinetic energy. It was estimated by the method outlined in reference 4. $\langle E_\gamma \rangle$ was taken to be 8.2 MeV.

Table B gives the various terms evaluated for all reactions studied in this work. It also gives the final values of $\langle \nu_T \rangle$.

Table B. Average number and kinetic energy of neutrons from fission fragments.

System	Bombarding Energy (MeV)	$\langle E_R \rangle$ (MeV)	$\langle B_n \rangle$ (MeV)	$\langle E_n \rangle$ (MeV)	$\langle \nu_T \rangle$
$_{68}Er^{170} + _8O^{16}$	165	105.7	6.48	2.54	10.6
	151	105.7	6.48	2.37	9.4
	136	105.7	6.48	2.17	7.9
	120	105.7	6.48	1.92	6.1
$_{70}Yb^{174} + _6C^{12}$	125	105.7	6.48	2.09	7.3
	109	105.7	6.48	1.89	5.9
$_{74}W^{182} + _8O^{16}$	165	135.5	6.97	2.57	11.1
	144	135.5	6.97	2.35	9.3
	127	135.5	6.97	2.14	7.8
	115	135.5	6.97	1.97	6.5
	102	135.5	6.97	1.76	5.1

C. Errors in Transforming Data to Energy-Mass Distributions

It was seen in Section III-E that the exact expression for the transformation of two-dimensional energy data to mass-total kinetic energy distributions is given by

$$A_{1\,(exact)} = \frac{E_2 A_c}{E_T} \ . \qquad (C-1)$$

A_1 and E_2 are the mass and initial fragment energy respectively, E_T is the total kinetic energy released, and A_c is the mass of the compound nucleus. In the transformations used in this work, Eq. (C-1) has been replaced by

$$A_{1\,(approx)} = \frac{E_2^* A_c}{E_T^*} \ , \qquad (C-2)$$

where the stars are used to identify energies after neutron emission.

Table C illustrates the errors introduced by this assumption for the case of Os^{186} compound nucleus. It was compiled in the following way. An initial representative total kinetic energy, E_T^*, was chosen arbitrarily. Various values of E_2^*, ν_1, and ν_2 were chosen for illustration purposes. (ν_1 and ν_2 are the numbers of neutrons emitted from fragments 1 and 2 respectively.) $A_{1\,(approx)}$ was evaluated using Eq. (C-2). The result was used to evaluate E_2 and E_T using the formulae of Section III-I. E_2 and E_T were then used in Eq. (C-1) to give $A_{1\,(exact)}$.

The difference between $A_{1\,(exact)}$ and $A_{1\,(approx)}$ appears to be within one mass unit for most events in any

Table C. Effect of neutrons on calculation of masses
of fission fragments.

E_1^* (MeV)	E_2^* (MeV)	ν_1	ν_2	E_T (MeV)	E_2 (MeV)	A_1 (approx)	A_1 (exact)
122	61	5	5	128.9	64.5	93	93
122	61	4	5	128.2	63.7	93	93
122	61	4	6	128.9	63.7	93	92
122	61	3	5	127.5	63.0	93	92
122	61	3	7	128.9	63.0	93	91
122	45	5	5	128.9	48.5	69	70
122	75	5	5	128.9	78.5	114	113
110	55	5	5	116.2	58.1	93	93
110	55	4	6	116.2	57.5	93	92

given distribution. Deviations of greater than one mass unit occur only for very asymmetric events or for relatively rare events in which one fragment for some reason emits several more neutrons than the other.

D. Theoretical Formula for Total Kinetic Energy-Mass Distributions

The approximate expression for the probability $N(E_T, A_1)$ of observing a given fragment total kinetic energy E_T and a given mass A_1 is given from the work of Nix[39] by

$$N(E_T, A_1) \cong \frac{E_o F(E_T, A_1)}{A \alpha \pi \sqrt{C_s C_m}} \left(\frac{A_1 A_2}{(A/2)^2} \right) \frac{1}{E_T^2} \exp\left[\frac{\left(\frac{A_1}{A} - \frac{1}{2} \right)^2}{C_m} - \frac{\left(\frac{E_o}{E_T} \frac{A_1 A_2}{(A/2)^2} - 1 \right)^2}{\alpha^2 C_s} \right],$$

where $A_2 = A - A_1$ and A is the mass of the compound nucleus. The constant E_o is the total kinetic energy that results when the initial condition is the most probable one (i.e., starting at rest from the saddle point), and α is a calculable constant that is related to the separation distance of two effective point charges having an interaction energy E_T. In appropriate units, E_o and α are functions only of the fissionability parameter x. The calculable constants C_s and C_m give the widths of the initial distributions in the vibrational degree of freedom corresponding to a symmetric stretching of the nucleus, and the mass asymmetry degree of freedom respectively. The temperature dependence of these constants is given from references 3 and 39 by

$$C_s = \frac{\hbar \omega_s}{K_s} \coth \frac{\hbar \omega_s}{2 \theta} \longrightarrow \begin{cases} 2\theta/K_s, & \theta \gg \hbar \omega_s \\ \hbar \omega_s/K_s, & \theta \ll \hbar \omega_s \end{cases}$$

$$C_m = \frac{2 \theta}{K_m}$$

where the frequency ω_s and the stiffness constants K_s and K_m are non-adjustable parameters that are calculated from the theory. The distributions in initial conditions are seen to

broaden with the temperature θ, which in turn broadens the final observed distribution. The factor $F(E_T, A_1)$ has a complicated F_T and A_1 dependence, but its value is always close to unity for the cases studied here.

E. Rotational Parameters

This appendix is intended to show how certain rotational quantities can be calculated from the specified conditions of bombardment.

1. Maximum Angular Momentum L_{max}

Let E_{cm} be the energy of the projectile in the center-of-mass system. To obtain a value for L_{max}, we assume that E_{cm} will be equal to the sum of the Coulomb barrier, and the maximum centrifugal barrier. Thus,

$$E_{cm} = \frac{Z_T \, Z_P \, e^2}{R_T + R_P} + \frac{L_{max}(L_{max} + 1)}{2\mu (R_T + R_P)^2} \quad , \qquad (E1)$$

where Z is the atomic number, e the electron charge, R the nuclear radius, L_{max} the maximum angular momentum, and μ the reduced mass $(\mu = \frac{mA_P A_T}{A_P + A_T}$, where m is the nucleon mass). The subscripts P and T refer to the projectile and the target respectively.

Thus, assuming 1 to be very small when compared with L_{max}, we have

$$L_{max} \cong (R_T + R_P) \sqrt{2\mu (E_{cm} - V_c)} \quad , \qquad (E2)$$

where V_c is the Coulomb barrier. Thus the value of L_{max} depends on the nuclear radii R_T and R_P.

2. Maximum Rotational Parameter y_{max}

The rotational parameter y has been defined in the main body of the text as

$$y = E_R^{\,o}/E_S^{\,o} \quad .$$

Using $E_s^o = 17.81 \, A^{2/3}$, we have for the compound nucleus

$$y = \frac{L(L+1)}{2 \mathcal{J}_o} / 17.81 \, A_c^{2/3} \quad , \tag{E3}$$

where $\mathcal{J}_o$ is the moment of inertia of a sphere and $A_c = A_P + A_T$. $\mathcal{J}_o$ is given by

$$\mathcal{J}_o = 2/5 \, m \, A_c R_c^2 \quad . \tag{E4}$$

Using $R = r_o A^{1/3}$ (where r_o is the radius parameter), Eq. (E4) becomes

$$\mathcal{J}_o = 2/5 \, m r_o^2 A^{5/3} \quad . \tag{E5}$$

Using the approximation $L(L+1) \approx L^2$ and evaluating expression (E3) at L_{max}, we have

$$y_{max} = \frac{L_{max}^2}{2 \mathcal{J}_o} / 17.81 \, A_c^{2/3} \quad . \tag{E6}$$

Using Eq. (E2) for L_{max} and Eq. (E5) for $\mathcal{J}_o$, and substituting $(A_T E_{lab}/A_T + A_P)$ for E_{cm} (E_{lab} is the bombarding energy in the laboratory system), Eq. (E6) becomes

$$y_{max} \approx \frac{5 \, A_P (1 + \left(\frac{A_P}{A_T}\right)^{1/3})^2 \left[\left(\frac{1}{1+A_P/A_T}\right)E_{lab} - B\right]}{2 \, A_T^{5/3} (1+A_P/A_T)^{10/3} \quad 17.81} \quad . \tag{E7}$$

This result is independent of r_o. Since the fission barrier is a function of y, its value for any given case does not depend on the choice of r_o.

3. Rotational Energy

Rotational energy, E_R, is defined by

$$E_R = \frac{L(L+1)}{2 \mathcal{J}} \quad ;$$

$$E_R \simeq \frac{L^2}{2\mathcal{J}} \qquad .$$

The rotational energy of a sphere is $E_R^{\,o}$, and from the definition of y, it may be calculated by

$$E_R^{\,o} = 17.81 \ y \ A_c^{\,2/3} \qquad . \qquad (E8)$$

Thus again $E_R^{\,o}$ is independent of r_o provided the accepted value of $17.81 \ A^{2/3}$ is used for $E_s^{\,o}$.

4. Probability of Obtaining an Angular Momentum between L and L+dL

Let R be the maximum value of the impact parameter r at which a projectile is able to form a compound nucleus with a spherical target. From a simple geometrical argument, it may be shown that for such a reaction the probability of the impact parameter being between r and r+dr is given by

$$\text{probability} = \frac{2rdr}{R^2} \qquad . \qquad (E9)$$

If p is the linear momentum of the projectile, the angular momentum of the resulting system, L, is given by

$$L = pr \qquad .$$

Therefore , $dL = pdr$.

For the maximum case,

$$L_{max} = pR \qquad .$$

Substituting in (E9), we find that the probability of obtaining an angular momentum between L and L+dL is given by

$$\text{probability} = \frac{2LdL}{L_{max}^{\,2}} \qquad .$$

F. Burnett's Neutron Correction Formulae

The following formulae have been used in this work to correct the moments of the distributions. They were derived by Burnett[4], and their derivation is outlined in the appendix to reference 4. The asterisk is used to denote the uncorrected quantity. The subscripts 1 and 2 denote the two fragments. ν_T is the number of neutrons emitted, m is the nucleon mass and $\langle E_n \rangle$ the average kinetic energy of the neutrons emitted. The corrected average total kinetic energy, $\langle E_T \rangle$ is given by

$$\langle E_T \rangle \simeq \langle E_T^* \rangle \left[1 + \frac{\nu_T}{2A} \left(\frac{A_1}{A_2} + \frac{A_2}{A_1} \right) \right] \ .$$

The corrected variance of the kinetic energy distribution is given by

$$\mu_2(E_T) \simeq \left[\mu_2(E_T^*) - \frac{4}{3} \frac{m}{A} \langle E_T \rangle \langle E_n \rangle \frac{\nu_T}{2} \left(\frac{A_1}{A_2} + \frac{A_2}{A_1} \right) \right] \left[1 - \frac{\nu_T}{2A} \left(\frac{A_1}{A_2} + \frac{A_2}{A_1} \right) \right]^{-2} \ ,$$

and the corrected variance of the mass distribution is given at a given E_T^* by

$$\mu_2(A_2) \simeq \left(\mu_2^*(A_2) - \nu_T \, mA \, \frac{\langle E_n \rangle}{E_T^*} \right) \left(1 - \frac{2\nu_T}{A} \right)^{-1} \ .$$

-89-

ACKNOWLEDGMENTS

It is a pleasure to acknowledge my indebtedness to
Dr. Stanley G. Thompson. He has suggested this research
problem, and his continued help, guidance, and interest
during the course of this work have been invaluable.

My sincere thanks go to Dr. Wladyslaw J. Swiatecki,
who has been a source of inspiration to me during this work.
His collaboration on the theoretical phases are greatly
appreciated.

I am grateful to Dr. Isadore Perlman for continued
interest in this research.

I wish to thank Drs. Donald S. Burnett and Eldon L.
Haines for help during the long experimental hours and for
many fruitful discussions.

Discussions with J. Rayford Nix, Dr. Torbjørn Sikkeland,
Dr. Victor E. Viola, Dr. Reinhard Brandt, and Harry R. Bowman
have been very helpful.

The help of Leonard E. Gibson and William W. Goldsworthy
in setting up and maintaining the electronic system was
essential.

I wish to thank Daniel J. O'Connell for preparing the
targets used in this work.

My thanks go to Dr. Torbjørn Sikkeland for the use of
his fission chamber at a time when he also used it for a
series of experiments and for the permission to use his fission

cross section data.

The collaboration of Dr. Stanley Cohen during the course of the liquid drop calculations is appreciated.

The help of Mrs. Joan Phillips, Mr. David Ijams, and Mrs. C. M. Goldenberg in the preparation of this manuscript is gratefully acknowledged.

FOOTNOTES AND REFERENCES

1. V. M. Strutinskii, N. Ya. Lyashchenko, and N. A. Popov, Soviet Physics JETP $\underline{16}$, 418 (1963).

2. S. Cohen and W. J. Swiatecki, Ann. Phys. $\underline{22}$, 406 (1963).

3. J. R. Nix, in Proceedings of the Third Conference on Reactions between Complex Nuclei (University of California Press, Berkeley, 1963).

4. D. S. Burnett, University of California Radiation Laboratory Report UCRL-11006, October 1963.

5. E. L. Haines, University of California Radiation Laboratory Report UCRL-10342, June 1962.

6. The Au^{197} + He^4 experiment was carried out jointly with D. S. Burnett. The results are given in reference 4.

7. Targets have been prepared by the method of electron bombardment by Daniel J. O'Connell and co-workers.

8. T. Sikkeland, E. L. Haines, and V. E. Viola, Phys. Rev. $\underline{125}$, 1350 (1962).

9. T. Sikkeland and V. E. Viola, in Proceedings of the Third Conference on Reactions between complex Nuclei (University of California Press, Berkeley, 1963).

10. E. L. Hubbard, et. al, Rev. Sci. Instr. $\underline{32}$, 621 (1961).

11. L. C. Northcliffe, Phys. Rev. $\underline{120}$, 1744 (1960).

12. J. L. Blankenship, Surface Barrier Detectors, in Semiconductor Nuclear Particle Detectors, Proceedings of an Informal Conference (National Academy of Sciences-National Research Council, Washington, D. C., 1961), Publication 871.

13. See for example H W. Schmitt, et. al., Response of
    Silicon Solid-State Detectors to Heavy Ions and Fission
    Fragments, in Physics Division Annual Report, ORNL-3425
    p. 130; and also reference 4 and 5 above.

14. V. E. Viola and T. Sikkeland, University of California
    Radiation Laboratory Report UCRL-10284, October 1962.

15. V. E. Viola and T. Sikkeland, private communication.

16. W. W. Goldsworthy, University of California Radiation
    Laboratory Report UCRL-9816, August 1961.

17. Lawrence Radiation Laboratory Counting Handbook,
    UCRL-3307 Rev., January 1959, File CC-10-2.

18. The fast electronic system used during this work has
    been designed by W. W. Goldsworthy.

19. Ref. 17, File CC-1-4.

20. Ref. 17, File CC-3-10.

21. Ref. 17, File CC-3-11.

22. J. M. Alexander and M. F. Gazdik, Phys. Rev. 120, 874
    (1960).

23. The center-of-mass correction used in this work is des-
    cribed in Part B of the appendix of reference 5.

24. T. D. Thomas and W. M. Gibson, Transformation of Two-
    Dimensional Data Princeton-Pennsylvania Accelerator,
    PPAD 473 E, October 1962.

25. The random number method used in this work has been pro-
    grammed for the IBM 7094 computer by D. S. Burnett.

26. J. C. D. Milton, University of California Radiation Laboratory Report UCRL-9883 Rev., January 1962.

27. R. B. Leachman, in _Proceedings of the Second International Conference on the Peaceful Uses of Atomic Energy_ (United Nationa, Geneva, 1958), Vol. 15, p. 229.

28. T. Sikkeland, unpublished results. These results were found to be consistent with similar results of J. Gilmore et. al., University of California Radiation Laboratory Report UCRL-9304 Rev., June 1962.

29. G. A. Pik-Pichak, Soviet Physics JETP $\underline{7}$, 238 (1958).

30. The name Hiskes shape has been suggested in reference 33. Hiskes has studied the shapes of stable equilibrium of rotating charged drops, and his results are given in reference 41.

31. These calculations have been performed in collaboration with W. J. Swiatecki and S. Cohen.

32. The fissionability parameter x may be defined in the following two ways:
$$x = E_c^{\,0}/2E_s^{\,0} \quad ,$$
where $E_c^{\,0}$ and $E_s^{\,0}$ are the Coulomb and surface energies of a sphere respectively, and
$$x = (Z^2/A)/(Z^2/A)_{crit} \quad .$$
The value for $(Z^2/A)_{crit}$ of 50.13 is usually found in the literature. Recent experiments,[46] however, indicate that perhaps a better value for $(Z^2/A)_{crit}$ is 48.4. Since it

is not known how this change from 50.13 to 48.4 would be distributed between the surface and Coulomb energies, the old value of 50.13 was used throughout this work, except where otherwise stated. The virtue of this procedure was that a set of self-consistent constants was used throughout the work.

33. S. Cohen, F. Plasil, and W. J. Swiatecki, University of California Radiation Laboratory Report UCRL-10775, April 1963.

34. G. A. Pik-Pichak, Soviet Physics JETP 16, 1201 (1963).

35. J. F. Mollenauer, private communication.

36. S. Cohen and W. J. Swiatecki, Ann. Phys., 19, 67 (1962).

37. Quantitative aspects of the rotating liquid drop calculations will be reported in a later paper.

38. B. C. Carlsan and Pao Lu, Proceedings of the Rutherford Jubilee International Conference, 291 (1962).

39. J. R. Nix, Ph. D. Thesis, University of California Radiation Laboratory Report in preparation.

40. J. R. Nix, private communication.

41. J. R. Hiskes, University of California Radiation Laboratory Report UCRL-9275, June 1960.

42. R. Beringer and W. J. Knox, Phys. Rev. 121, 1195 (1961).

43. J. R. Huizenga and R. Vandenbosch, Nuclear Fission, Nuclear Reactions Volume II (North Holland Publishing Company, 1962).

44. J. M. B. Lang and K. J. Le Couteur, Proc. Phys. Soc. (London) A65, 592 (1954).

45. W. J. Swiatecki, Semi-Empirical Interpretation of Nuclear Masses and Deformation (Talk presented at the Vienna Conference on Nuclear Masses, August 1963).

46. D. S. Burnett, R. C. Gatti, F. Plasil, P. B. Price, W. J. Swiatecki, and S. G. Thompson, University of California Radiation Laboratory Report UCRL-11079, November 1963.

47. H. C. Britt and A. R. Quinton, Phys. Rev. 120, 1768 (1960) and also Phys. Rev. 124, 877 (1961).

48. J. R. Huizenga, R. Chaudhry, and R. Vandenbosch, Phys. Rev. 126, 210-219 (1962).

49. B. R. Mottelson and J. G. Valatin, Phys. Rev. Letters, 5, 511 (1960).

50. G. N. Simonoff and J. M. Alexander, in Proceedings of the Third Conference on Reactions between Complex Nuclei, (University of California Press, Berkeley, 1963).